Marine Structures 75 (2021) 102886

Contents lists available at ScienceDirect

Marine Structures

journal homepage: http://www.elsevier.com/locate/marstruc

Mean and unsteady loading on square prisms with rounded edges: Hard marine growth, incidence, and Reynolds number effects

Nils Paul van Hinsberg

Institute of Aeroelasticity, German Aerospace Center, Göttingen, Germany

ARTICLE INFO

Keywords:
Bluff body
Edge roundness
Reynolds number
Flow separation
Marine growth
Aerodynamics
Surface roughness
Square prism

ABSTRACT

A set of wind tunnel experiments was performed to study the average and fluctuating wind loading on an "infinite" 2D square prism with rounded edges of $r/D = 0.16$ for different heights of simulated hard marine growth at sub-to transcritical Reynolds numbers. It has already been shown, that a change in surface roughness from $k_s/D = 4.5 \times 10^{-6}$ (smooth) to 1×10^{-3} (rough) on a similar prism at $\alpha = 0^\circ$ and 45° had large effects on the widths and the Reynolds numbers marking the boundaries of the various flow states. At $\alpha = 45^\circ$ it furthermore led to a large Reynolds-number independency of the lift and drag forces and of the Strouhal number. For the present wind tunnel tests two additional values of k_s/D were selected to obtain smaller increments in surface roughness: 4.5×10^{-4} (slightly rough) and 1.4×10^{-3} (very rough). Mean and fluctuating lift and drag forces, the main vortex shedding frequency, distributions of the mean surface pressures in the mid-span cross-section of the prism and the mean wake profiles were recorded simultaneously. The same two static angles of incidence, $\alpha = 0^\circ$ and 45°, were investigated for $Re_D = 60{,}000$–12 million. For the prisms with smooth up to rough surfaces strong effects on the behaviour of all aerodynamic parameters with Reynolds number were found, whereas a further increase in k_s/D induced hardly any additional effects. The absolute values of the aerodynamic parameters were found to be independent of a change in k_s/D for the sub-to supercritical flow states. For the smooth and slightly rough prisms at $\alpha = 0^\circ$ the supercritical flow state was present up to $Re_D = 12$ million, whereas for the rougher prisms the upper transition and the transcritical flow states appeared at high Reynolds numbers. A change to $\alpha = 45^\circ$ induced little variation with k_s/D for all aerodynamic coefficients. The overall behaviour of the force coefficients and the Strouhal number with k_s/D and Re_D were caused by motions of the transition, separation and reattachment locations.

1. Introduction

The strong energy revolution the world is currently going through results in an increasing use of wind as a reliable source of energy. This conversion includes, among other things, the planning and realisation of new and the expansion of existing wind farms, both on- and offshore. Owing to the growing demand for clean energy and the climate goals of the European Union [1,2], the manufacturers of wind power plants are constantly confronted with new challenges. To increase the energy yield of the wind turbines to an optimum and the costs per delivered MW for the manufacturing of the different components and the erection of the wind turbines to a minimum, the rotor diameters and the tower heights of modern horizontal axis wind turbines are being increased and the locations of new offshore

E-mail address: nils.vanhinsberg@dlr.de.

https://doi.org/10.1016/j.marstruc.2020.102886
Received 14 April 2020; Received in revised form 4 July 2020; Accepted 6 September 2020
Available online 30 October 2020

wind farms are more and more being shifted away from the shore and shallow water into the deep sea to capture faster, more consistent winds with less turbulence [3,4]. Besides these economical factors social aspects, like visual and noise pollution and shadow flicker, are also seen as important driving forces behind the expansion of offshore wind farms.

1.1. Influence of marine growth

Following their placement in the ocean, no matter whether in relatively shallow waters or further offshore in the deep sea, the submerged parts of offshore wind turbines function as artificial reefs. They are colonised by marine microorganisms which leads over the years to the settlement of a bright variety of marine fouling organisms [5–8]. Water depth [5,9] and temperature, ocean current, foundation design, penetration depth of sunlight, geographical location, distance from the coast line, support surface and the season [7] are, among others, influencing factors on the distribution on the submerged members. Three main categories of marine growth can be distinguished, namely hard growth (e.g. oysters, tubeworms, mussels), soft growth, like sponges, anemones, algae, sea-squirts, seaweeds, and kelp growth, a long flapping weed [6,7]. As a consequence of the marine growth, the flow around these parts of offshore renewables is steadily being altered during their lifetime. Eventually this may lead to large economical and technical problems, like lower fatigue life of the mooring lines [10] and mask effects for inspection methods for possible cracks and corrosion on the pillars of the foundation structures.

From an engineering perspective bio colonisation has a number of effects on the hydrodynamic properties of the immerged slender structures. It leads, for example, to hydrodynamic overloading as a result of the increased structural diameter - hence, both larger lift and drag forces and increased hydrodynamic added masses - of the displaced volume and of the increased mass. The weight increase, in combination with the larger hydrodynamic added mass, furthermore lowers the natural frequency of the structure. In particular for mooring lines, with their relatively small diameters compared to the main columns of the floating structure, this can move their structural responses to resonance. In Ref. [11] it was for example shown that the natural frequency of both the front and rear mooring lines ($D = 0.19$ m) of a 2 MW floating wind turbine was cut by half when the uniformly distributed marine growth was increased by only 80 mm. The added surface roughness also affects the mechanism of vortex formation, thereby increasing both the vortex strength and their spanwise coherence, thus giving rise to even higher periodic lift forces [12] which may lead to a further increase of the susceptibility towards vortex-induced vibrations. Another problem of marine fouling, which should not be underestimated, is its required removal on (parts of) the outer surfaces of the submerged foundations before routine inspections can be carried out. One possible way of reducing marine fouling is to cover the outer surfaces with anti-fouling paints. The main problem thereby is, that most of the paints used in the past were toxic, as a result of which they have gradually disappeared from the market again. Currently, non-toxic anti-fouling paints based on for example physico-chemical strategies or enzymes are being developed, which will be available in the near future [8,13,14]. Another method to prevent marine growth is the use of anti-fouling hoops and brushes: the sea current sets the hoop into a spiral motion and the additional steel or nylon brushes remove the marine fouling. This method only works for cylindrical structures though. A regular inspection and manual removal of marine fouling by hand tools or water jets, although costly, is therefore currently the only environmental-friendly solution to keep the marine growth on prismatic members under control.

Only a limited number of studies are available on the effect of marine fouling on the hydrodynamic behaviour of offshore wind turbines and other marine structures. Jusoh and Wolfram [9], for example, discussed the various effects marine growth has on the hydrodynamic loading on offshore structures. They stated that *"the most important state of loading exerted on offshore structure comes from hydrodynamic action which are influenced by C_D and C_M values"*. In Ref. [15] a modelling of marine growth effects based on both the Response Surface Methodology and experiments on a jacket platform in the North Sea was presented. With this method an approximation of the structural response - in terms of hydrodynamic loading coefficients on offshore structures - to extreme events or fatigue loading was given. The effect of thickness, density and values of hydrodynamic coefficients of marine growth on the characteristics of an offshore wind turbine having a jacket platform were studied by Shi et al. [16]. Their analysis of the eigenmodes and eigenfrequencies showed that marine fouling has in particular an effect on the second and third order natural frequencies of the jacket structure. They furthermore found that both the density and the thickness of marine growth strongly influence the hydrodynamic loading on the structural components. A numerical study by Wright et al. [17] also showed a notable influence of marine growth of various thickness and surface roughness on the hydrodynamic forces on a tension moored PelaStar floating wind turbine. Whereas an increase in marine growth thickness induced on the one hand lower surge motions, pitch motions and nacelle accelerations, it introduced larger maximum and lower minimum tendon forces on the other hand. In particular the latter phenomenon, i.e. a considerable decrease of the tendon force on the vertical taut mooring lines, could lead to the so-called slack tendon event, at which point a tendon loses all tension and undesirable snap loading can occur. To avoid this undesired effect they concluded that a maximum of 80 mm of marine growth on the mooring lines should not be exceeded for this specific wind turbine. A quite recent experimental study by Henry et al. [18] focused on the effects of hard and soft marine fouling on the mean drag force and the wake structure of a circular cylinder at Reynolds numbers between 2.16×10^3 and 1.94×10^4, by using a load cell and the Particle Image Velocimetry (PIV) measurement technique. They observed that an increase in non-dimensional height of the hard roughness from $k/D = 0$ up to $k/D = 0.07$ induced a slight increase in drag force and a reduction of the vortex shedding frequency, whereas the width of the vortex street first increased with larger surface roughness, before decreasing at the largest investigated hard roughness. Soft fouling, on the other hand, was found to act as a passive flow separation control: the artificial fur stabilised the cylinder wake, which led to an increase of the length of the recirculation region by a factor five in comparison to hard fouling and a significant reduction of the vortex shedding frequency. Hence, the conditions of the occurrence of vortex-induced vibrations could thus be modified in a passive way.

1.2. Effect of hard surface roughness on circular cylinders

One way of representing hard marine fouling like oysters, tubeworms, barnacles, and mussels in wind tunnel or water tunnel lab experiments is by covering the outer surfaces of the (scaled) structure with a roughness which is characterised through its non-dimensional equivalent sand-grain surface roughness, k_s/D. The possible effects of surface irregularities on the dynamic loading of and the flow topology around 2D (infinite) circular cylinders in steady cross-flows have been extensively studied and well documented [19–32]. However, in most of these studies the main emphasis was not placed on the influence of marine growth on the hydro- and aerodynamic behaviour of circular cylinders. The applied surface roughness was in fact only used as a passive instrument to provoke an artificial transition and an earlier separation of the surface boundary layer in order to simulate high-Reynolds-number flow phenomena at physically low Reynolds numbers. The mean drag force and the vortex shedding frequency up to the supercritical/upper transition flow state (see Section 2 for a detailed description of the various flow states) were for example studied in Refs. [23,28–33] by applying uniformly distributed dimples and grooves at the cylinder surface. To simulate the flow phenomena around a circular cylinder in the transcritical Reynolds-number regime, Ribeiro [34] used span-wise roughness stripes at a single angular position or at multiple circumferential angles. The same principle was applied in the numerical study by Behara and Mittal [35] to promote an early transition of the boundary layer on the upper half of a smooth cylinder. To reach higher Reynolds numbers in their experiments, Fage and Warsap [19], Batham [21], Szechenyi [22] and Güven et al. [24] covered the complete cylinder surface with solid particles, like glass beads, or with large sheets of glass or sand paper. The data of all of these studies clearly showed that not only the (ir)regular texture and the relative height of the surface roughness, but also its location on the outer surface have a significant effect on the loading on circular cylinders, in particular in the critical and supercritical flow states. The main reason can be found in the behaviour of the surface boundary layer on the cylinder with increasing surface roughness. A higher surface roughness leads to a shift of the transition locations towards lower circumferential angles and an earlier separation of the turbulent boundary layer from the cylinder's surface, hence a wider near wake and higher supercritical and transcritical mean drag coefficients. An exception forms the subcritical flow state with high mean drag coefficients being independent of the surface roughness height.

The interchangeability in effect between Reynolds number and surface roughness, which is often given as a justification for examining high-Reynolds number flow phenomena, is questionable though. Particularly in the critical and supercritical Reynolds-number ranges the outcome of the measurements is sensitive to even the smallest disturbances in the flow conditions and in the local model surface topology [36]. This is for example the case for the transition and separation positions of the boundary layer on the surface of the cylinder, the three-dimensionality of the flow along the span of the cylinder and the vortex shedding in the wake, and thus also for the overall induced aerodynamic forces. In Ref. [37] the effects of both influencing parameters, i.e. Reynolds number and cylinder's surface roughness height, were therefore decoupled by varying the air density inside the wind tunnel, while keeping all other boundary conditions like cylinder diameter, surface roughness and turbulence intensity constant. The results showed that for physical Reynolds numbers between 10^4 and 10^7 a change in surface roughness height from $k_s/D \sim 10^{-5}$ to 10^{-3} led to a shift of all flow states towards significantly lower Reynolds numbers, a reduction of the supercritical flow state to a single point and a recovery of the mean drag coefficient in the upper transition state. In the critical flow state the spanwise flow around the rougher cylinder was found to be strongly three-dimensional. Both cylinders furthermore exhibited an asymmetric bistable state with a one-sided separation bubble and typical hysteresis effects for critical Reynolds numbers [37,38].

1.3. Objective of the present study

To identify and understand the effect of hard marine fouling on the flow behaviour around submerged members of offshore wind turbines, this study focuses on the main influences of the thickness of hard marine fouling on prisms with a square cross-section and rounded edges. These kind of cross-sectional shapes are found in particular as foundations of semisubmersibles [39–43], being one of the many hybrid floating platform configurations for offshore wind turbines in water depths larger than 50 m [44–46]. To the author's present knowledge the only experimental study that has focussed up to today on the influence of hard marine fouling on the loading on this kind of submerged members in a steady cross-flow has been performed by Ref. [47] for Reynolds numbers up to realistic values as high as 12 million. In that study it has been presented that an increase of the non-dimensional surface roughness height by a factor of $\mathcal{O}(10^3)$ on 2D initially smooth square prisms with non-dimensional edge radii of $r/D = 0.16$ and 0.29 (r being the radius of the spanwise edges and D the width of the prism) at $\alpha = 0^\circ$ and 45° resulted in similar trends of the behaviour of the flow as has already been mentioned in Section 1.2 for a 2D circular cylinder in Ref. [37]. For both incidence angles the transcritical flow state was for example already present at Reynolds numbers that lay for the corresponding smoother prism configurations still within the subcritical flow state. Whereas at $\alpha = 0^\circ$ the values of the fluctuating and mean force coefficients and of the main vortex shedding frequency were nearly independent of the surface roughness height, a change to $\alpha = 45^\circ$ led to a large Reynolds-number independency for the rougher prism. In particular the drag crisis and the following recovery in the upper transition flow state were affected.

Owing to the lack of further experimental and numerical data in this area and the large increment in the change in surface roughness in Ref. [47], a second experimental study has been performed to investigate the main influences of a smaller increment in the height of hard marine fouling on the flow behaviour around an "infinite" square prism with rounded edges of $r/D = 0.16$. For the present wind tunnel tests two additional values of k_s/D were selected to obtain smaller increments in surface roughness: 4.5×10^{-4} (slightly rough) and 1.4×10^{-3} (very rough). The aim of the experiment is to characterise the variations induced on the mean and fluctuating lift and drag forces, the vortex shedding frequency, the mean surface pressure distribution and the mean wake profile with changing surface roughness in high Reynolds-numbers flows of $Re_D = 60{,}000$–12 million. The two "symmetric" angles of incidence, i.e. $\alpha = 0^\circ$ and 45°, were investigated for different stages in the simulated process of hard marine growth.

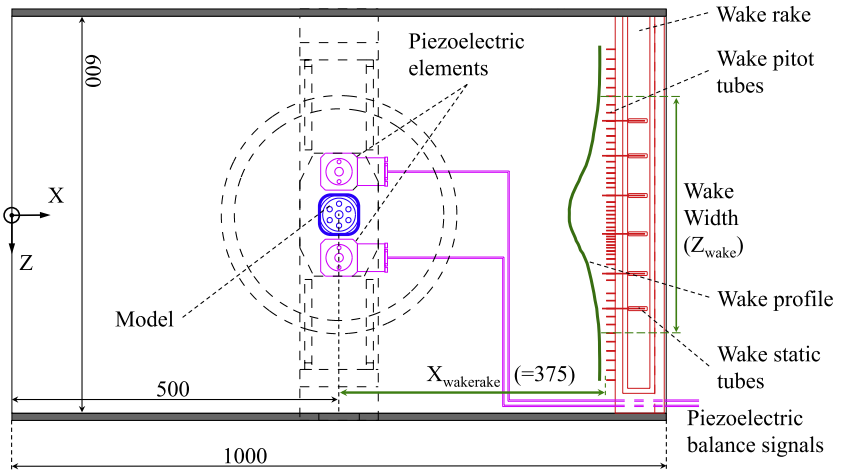

Fig. 1. Side view of the test section with positions of wind tunnel model, piezoelectric balances and wake rake (all dimensions in mm).

2. Terminology of the different flow regimes for high-Reynolds-number flows around two-dimensional cylinders and prisms

Based on the behaviour of the surface boundary layer and of the free shear layers, as well as the locations of the boundary layer separation and possible reattachment, four main high-Reynolds-number flow regimes can generally be defined for two-dimensional (”infinite”) circular cylinders in cross-flow: subcritical, critical, supercritical with upper transition and transcritical [23,38,48,49].

A boundary layer that remains laminar along the surface of the bluff body up to separation, a largely laminar shear layer, and a high and more or less steady mean drag coefficient, the latter being highly independent of the Reynolds number, characterises the first flow regime. In this flow state the Strouhal number has a constant value of about 0.2. In the critical Reynolds-number flow regime a moderate up to strong decrease and increase of, respectively, the mean drag coefficient (i.e. the ”drag crisis”) and the Strouhal number take place with increasing Reynolds number. At the critical Reynolds number at the end of this regime the lowest mean drag force and the highest Strouhal number are reached. With increasing Reynolds number within this flow state the location of the transition to turbulence flow shifts upstream along the free shear layer, as a result of which a shear layer reattachment can occur, thereby forming a separation bubble close to both shoulders of the cylinder. The attached turbulent boundary layer separates then again on the back portion of the cylinder and induces a lower negative mean base pressure and a smaller wake width, hence a lower mean drag force and a higher Strouhal number. A bistable state can occur in a small Reynolds-number range within the critical flow state, characterised by a one-sided separation bubble, a steady mean lift force on the circular cylinder, a clear three-dimensionality of the flow around the cylinder, and a hysteresis in the flow phenomena between increasing and decreasing Reynolds numbers (e.g. Ref. [37,38,50] and references therein). A low and relatively constant value of the mean drag coefficient, a high Strouhal number and the presence of two separation bubbles on the surface of the body define the supercritical flow regime. The change from supercritical to transcritical occurs in the upper transition and is accompanied by a decrease of the mean base pressure and an increase in the mean drag coefficient as a result of the upstream motion of the separation point of the turbulent boundary layer, a steady shrinkage of both separation bubbles, and the associated expansion of the wake. In the latter regime the transition to turbulence occurs in the vicinity of the stagnation point, hence far upstream of the boundary layer separation locations. A steady flow is formed around the cylinder and in its wake, thereby inducing a large independency on the Reynolds number of the mean base pressure, the mean and fluctuating aerodynamic force coefficients, and the Strouhal number.

In [47,51] it was shown, that, based on the trends of the curves of the mean and fluctuating aerodynamic coefficients and the Strouhal number versus Reynolds number, a similar division into these four main flow regimes can be applied to the

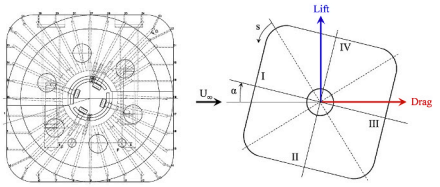

(a) Pressure tap distribution over the model's mid-span cross-section

(b) Numeration of side surfaces of the prism (*I-IV*), definitions of the aerodynamic vectors and incidence angle

Fig. 2. Distribution of the static pressure taps over the mid-span cross-section of the two-dimensional ”infinite” square prisms with rounded edges of $r/D = 0.16$, as well as the definitions of the aerodynamic load vectors, the side surfaces I-IV and the angle of incidence.

high-Reynolds-number data of two-dimensional smooth and (slightly) rough square prisms with rounded edges. The same terminology will therefore also be adopted in the following presentation and discussion of the current aerodynamic results.

3. Experimental approach

The wind tunnel test setup and the instrumentation were similar to those described in detail in Ref. [47,51]. The cross-section of test section of the closed return High Pressure Wind tunnel of the German-Dutch Wind Tunnels (DNW) was 0.6×0.6 m^2 and measured 1 m in length. A sketch of the side-view of this test section is shown in Fig. 1.

Through a combination of a pressurisation of the air inside the wind tunnel up to 10 MPa and a variation of the free stream velocity in the range $4 \leq U_\infty \leq 35$ maximum Reynolds numbers, based on the side width D of the square prisms, in the order of 10^7 could be achieved. Free stream turbulence intensities in the test section and the relative dynamic pressure variation across the working section at the prism's position were below 0.8% and 0.3%, respectively.

The square prisms had span lengths of $L = 600$ mm and common widths of $D = 60$ mm, hence their aspect ratios AR $= L/D$ were 10. All edges in spanwise direction had a roundness of $r/D = 0.16$, see Fig. 2a.

Each prism was fabricated through the assemblage of two stainless steel, partially hollow half models which were joined together with eight screws, equally distributed along the span of the model, after which the heads of the screws were removed by milling and their surfaces carefully machined and polished. Thereupon all four side surfaces of both prisms were covered with a plasmatic metal coating to obtain a Gaussian distributed non-dimensional equivalent sand-grain surface roughness - based on the algorithm by Ref. [52] - of $k_s/D = 4.5 \times 10^{-4} \pm 2 \times 10^{-5}$ or $1.4 \times 10^{-3} \pm 2 \times 10^{-4}$. These values represent the hard marine fouling after two different time periods upon placement of the offshore structures in the ocean. In Ref. [53] it has been discussed that the characterisation of hard marine growth by a single parameter k/D (or k_s/D) is not the most suitable solution, since other parameters, like the limitation of roughness scaling to model sizes, the percentage of coverage and the axial distribution have been shown to have a larger influence on the hydrodynamic loading and thus on the resultant fluid-structure interactions. However, up to date hardly any studies on the flow behaviour of submerged prismatic members of semisubmersibles under the influence of hard (and let alone soft) marine fouling have been performed. The approximation of hard marine growth by a surface sand roughness is therefore considered to be appropriate at this stage to gather first detailed information on the behaviour of this kind of foundation columns as function of the hard marine fouling height.

The prisms were mounted horizontally in the test section and spanned the complete width from one side wall to the other, whereby both ends of the model passed through the side walls of the test section. A labyrinth seal was used to minimise the amount of flow leakage through the small ring gaps between the model and the side walls. Thirty-six static pressure taps, with a diameter of 0.5 mm and equally spaced over the model's mid-span cross-section as shown in Fig. 2a, were used to obtain the mean surface pressure distribution with an uncertainty below 0.15% FS, hence ±150 Pa. Their positions on the surface of the prism are given by the non-dimensional circumferential coordinate s/D with $s/D = 0$ at the middle of the rounded edge between the surfaces *I* and *IV* according to Fig. 2b. The position in spanwise direction of each pressure tap hole was shifted by an amount of 1.65 mm with respect to its closest neighbours in order to avoid an interference of the local pressure at a tap hole position with the wake generated by the pressure holes located upstream. The dynamic calibration of the static pressure taps shows an upper cutoff frequency of about 860 Hz. The mean base pressure coefficient $C_{p,b}$ for $\alpha = 0^\circ$ was determined by taking the average of the pressure coefficient values obtained with nine taps located on surface *III* between $s/D = 1.91$ and $s/D = 2.74$, whereas 16 taps on the surfaces *III* and *IV*, hence at $2.02 \leq s/D \leq 3.57$, were used to determine $C_{p,b}$ at $\alpha = 45^\circ$. The global, hence spanwise integrated, lift $L(t)$ and drag $D(t)$ experienced by the prisms were

Table 1
Statistical signal information: minimum and maximum number of vortex shedding cycles for $T = 30$ s and number corresponding measurement points per shedding cycle.

α	k_s/D	f_L in Hz	No. shedding cycles	No. points/cycle
0°	4.5×10^{-6}	8.87	266	564
		172.53	5176	29
	4.5×10^{-4}	11.60	348	431
		154.90	4647	32
	1.0×10^{-3}	8.73	262	573
		85.00	2550	59
	1.4×10^{-3}	11.63	349	430
		95.37	2861	52
45°	4.5×10^{-6}	7.90	237	633
		88.17	2645	57
	4.5×10^{-4}	11.03	331	453
		74.10	2223	67
	1.0×10^{-3}	7.70	231	649
		72.20	2166	69
	1.4×10^{-3}	11.20	336	446
		70.20	2106	71

measured with two rigid piezoelectric platform balances, one positioned at each end of the wind tunnel model. The uncertainty of the recorded balance signals lay below 2%. The thereupon calculated global mean lift and drag coefficients are defined as $C_L = \overline{L(t)}/(q_\infty DL)$ and $C_D = \overline{D(t)}/(q_\infty DL)$ with $\overline{L(t)}$ and $\overline{D(t)}$ the mean values of respectively the lift and drag forces and q_∞ the free-stream dynamic pressure. The power spectra of the fluctuations of both force signals were computed to determine the main vortex shedding peaks and corresponding frequencies in lift and drag direction, hence f_L and f_D, respectively. The resulting Strouhal numbers were defined as $St_L = f_L D/U_\infty$ and $St_D = f_D D/(2U_\infty)$.

A vertical pressure rake with 6 static pressure tubes and 52 pitot pressure tubes was used to obtain the non-dimensional mean pressure loss in the near wake at 6.25 prism widths behind the model's spanwise centre axis, as shown in Fig. 1. This quantity is defined as $\Delta p = (p_0 - p_i)/q_\infty$, in which p_0 is the total pressure of the undisturbed flow and p_i the total pressure at location i (= 1, 2, …, 51, 52) in the near wake. The shape of the curve was analysed to extract the qualitative measure of both the (a)symmetry of the wake flow with respect to the model's horizontal spanwise axis and of the width of the near wake at this location. The latter is defined as the distance between the two most outer pitot pressure tubes for which the value of the non-dimensional pressure loss lies above the threshold of 4% of the maximum non-dimensional pressure loss, hence $\Delta p_{thr} = 0.04\Delta p_{max}$. The values evaluated for the pressures were assumed to have a 2% uncertainty.

In [37] it has been shown that in the asymmetric bistable flow state a clear three-dimensional pressure distribution exists along the span of the slightly rough circular cylinder with spanwise standard deviations as high as 43%. Since in the current test setup the model's surface pressure taps and the wake rake are positioned at, respectively downstream of the mid-span cross-section of the prism, the obtained pressure data are two-dimensional only. Hence, the presence of a three-dimensional flow, which is also likely to occur for square prisms with $r/D = 0.16$ at Reynolds numbers in the bistable flow state, cannot be demonstrated in the current study.

Two angles of incidence, $\alpha = 0^\circ$ and 45°, were investigated. The geometric wind tunnel blockage ratio was either 0.10 ($\alpha = 0^\circ$) or 0.13 ($\alpha = 45^\circ$). The formulas by Refs. [48,54] were applied to the measured free-stream velocity - and thus the Reynolds number, the Strouhal number and the three-dimensional mean and fluctuating lift and drag coefficients - and pressure coefficients, respectively, to correct for wall interference effects:

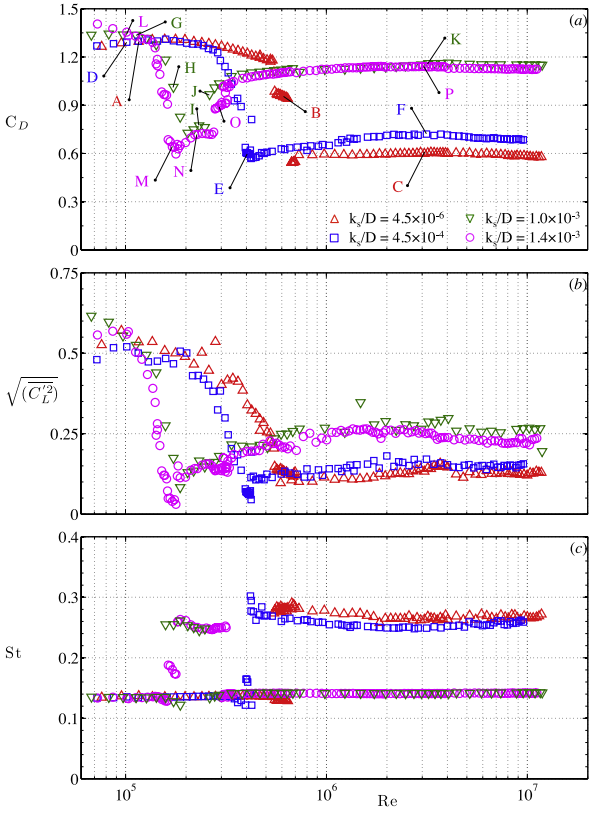

Fig. 3. Dependency of the mean drag coefficient, the fluctuations of the lift coefficient and the Strouhal number on the Reynolds number and surface roughness height for the two-dimensional square prism with rounded edges of $r/D = 0.16$ at an angle of incidence of $\alpha = 0^\circ$. Current data: □: $k_s/D = 4.5 \times 10^{-4}$ (*D*: subcritical, $Re_D = 1.0 \times 10^5$ - *E*: critical, $Re_D = 4.1 \times 10^5$ - *F*: supercritical, $Re_D = 3.2 \times 10^6$) and ∘: $k_s/D = 1.4 \times 10^{-3}$ (*L*: subcritical, $Re_D = 1.0 \times 10^5$ - *M*: critical, $Re_D = 1.7 \times 10^5$ - *N*: supercritical, $Re_D = 2.3 \times 10^5$ - *O*: upper transition, $Re_D = 2.9 \times 10^5$ - *P*: transcritical, $Re_D = 3.1 \times 10^6$); Van Hinsberg et al. [47]: △: $k_s/D = 4.5 \times 10^{-6}$ (*A*: subcritical, $Re_D = 1.2 \times 10^5$ - *B*: critical, $Re_D = 6.1 \times 10^5$ - *C*: supercritical, $Re_D = 3.1 \times 10^6$) and ▽: $k_s/D = 1.0 \times 10^{-3}$ (*G*: subcritical, $Re_D = 1.1 \times 10^5$ - *H*: critical, $Re_D = 1.7 \times 10^5$ - *I*: supercritical, $Re_D = 2.3 \times 10^5$ - *J*: upper transition, $Re_D = 2.6 \times 10^5$ - *K*: transcritical, $Re_D = 3.2 \times 10^6$).

$$U_{corr} = U_{uncorr}\left(1 + 0.25C_{D,balance,uncorr}\frac{A}{Z_{tunnel}} + 0.85\left(\frac{A}{Z_{tunnel}}\right)^2\right) \tag{1a}$$

$$C_{p,corr} = \left(C_{p,uncorr} - 1\right)\left(\frac{U_{uncorr}}{U_{corr}}\right)^2 + 1 \tag{1b}$$

with A the area of the prism subject to the flow and Z_{tunnel} the height of the test section. This resulted in maximum corrections in the order of 10%. Per measurement point a constant integration time of $T = 30$ s was chosen for all recorded signals; the aerodynamic forces were thereby scanned with a sampling frequency of $f_{scan} = 5$ kHz. The statistical signal information for each prism at both angles of incidence is summarised in Table 1, including the dominant frequency in the power spectra of the lift fluctuations, f_L, the number of total recorded shedding cycles over the integration period of $T = 30$ s and the amount of data points per vortex shedding cycle. In the current study the fewest number of cycles were 262 and 231 for $\alpha = 0°$and 45°, respectively, whereas the minimum number of measurement points per cycle were 29 ($\alpha = 0°$) and 57 ($\alpha = 45°$). Their values are sufficiently large to guarantee a precise calculation of the mean aerodynamic forces and their fluctuations, the mean surface pressure distribution, and the Strouhal number.

4. Experimental results

4.1. Variation in simulated hard marine growth thickness for $\alpha = 0°$

The combined effects of the non-dimensional hard marine fouling thickness - $k_s/D = 4.5 \times 10^{-6}$ (smooth), 4.5×10^{-4} (slightly rough), 1.0×10^{-3} (rough) and 1.4×10^{-3} (very rough) - and the Reynolds number on the mean drag coefficient C_D, the fluctuations of the lift force $\sqrt{(\overline{C_L'^2})}$, the Strouhal number St_L, and on the mean base pressure coefficient $C_{p,b}$ of the prism at $\alpha = 0°$ are presented hereafter. It will be shown that the value of k_s/D has a very distinct influence on the Reynolds-number-dependent behaviour of each of these aerodynamic parameters up to about $k_s/D \approx 1 \times 10^{-3}$, whereas a further increase in surface roughness beyond this value has barely any additional influence anymore. The general trends are a decrease of the lengths of the various flow states with increasing roughness thickness and the appearance of the upper transition and the transcritical flow states for the two largest surface roughness heights. For Reynolds numbers larger than 5×10^5 - 6×10^5 this leads to a strong increase in mean drag and a decrease of the vortex shedding frequency, both by about a factor 2, the latter being combined with a doubling of the lift fluctuations and a more intensified shedding process.

4.1.1. Aerodynamic loading

Fig. 3a shows the variation in C_D with Reynolds number at $\alpha = 0°$ for different values of the simulated hard marine fouling thickness k_s/D. The curve for $k_s/D = 4.5 \times 10^{-6}$ can be seen as reference curve for the smooth submerged members of a semisubmersible offshore wind turbine right after placement in the ocean.

Up to about $Re_D = 4 \times 10^5$ - 5×10^5 the subcritical flow state is present, characterised by a more or less constant high value of $C_D = 1.25$–1.3 for $Re_D \leq 2 \times 10^5$ and a subsequent steady, but still relatively small decrease in C_D up to the end of this flow state. The two typical sudden drops of the mean drag coefficient, the first one at $Re_D = 5.4 \times 10^5$ to a nearly constant intermediate level of $C_D \approx 0.95$–1.0 and the second one at $Re_D = 6.4 \times 10^5$ to its minimum value of $C_D \approx 0.55$, denote the critical flow state. This phenomenon, the so-called *drag crisis*, is characterised by its complex flow physics, like the possibility of the appearance of an asymmetric laminar separation bubble with a steady mean lift force within a small intermediate flow state and the dynamic behaviour of the transition and separation locations on the surface of the prism [47,51]. For $Re_D \geq 7 \times 10^5$ the constant low mean drag coefficient of 0.6 characterises the supercritical flow state.

The mean drag coefficient belonging to the slightly rough prism with $k_s/D = 4.5 \times 10^{-4}$, hence a hard marine growth height of $\mathcal{O}(10^2)$ larger than the smooth case, exhibits a similar trend with Reynolds number as described above for the smooth prism, but the drag crisis appears earlier, as a result of which the supercritical flow state starts already at $Re_D \approx 4 \times 10^5$. In the latter flow state C_D

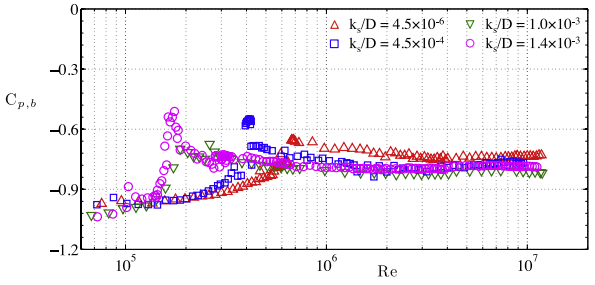

Fig. 4. Mean base pressure coefficient as function of the Reynolds number and the surface roughness height for the two-dimensional square prism with rounded edges of $r/D = 0.16$ at an angle of incidence of $\alpha = 0°$. Current data: □: $k_s/D = 4.5 \times 10^{-4}$ and ∘: $k_s/D = 1.4 \times 10^{-3}$; Van Hinsberg et al. [47]: △: $k_s/D = 4.5 \times 10^{-6}$ and ▽: $k_s/D = 1.0 \times 10^{-3}$.

performs a slight increase with Reynolds number from $C_D = 0.57$ at $Re_D = 4 \times 10^5$ up to its local maximum of 0.72 around $Re_D = 3 \times 10^6$ and remains at about this value up to $Re_D = 10$ million.

Doubling the height of the marine fouling to and beyond $k_s/D = 1.0 \times 10^{-3}$ tends to shift the boundaries of the critical flow state and thus the beginning of the supercritical flow state towards even lower Reynolds numbers. Interestingly, the slope of the drag crisis remains nearly constant. This same behaviour has been documented by many authors for "infinite" 2D circular cylinders with increasing surface roughness height, e.g. Refs. [23,24,28,29,37]. The most striking phenomena of the $C_D(Re_D)$-curves for the rough and very rough prisms are the limited length of the supercritical flow state with low values of C_D, the subsequent steep increase of the mean drag coefficient over a relatively short Reynolds-number range (i.e. the upper transition flow stage) which includes a large jump upwards in C_D at $Re_D = 2.5 \times 10^5$ and 2.8×10^5 for $k_s/D = 1.0 \times 10^{-3}$ and 1.4×10^{-3}, respectively, and the nearly constant plateau of C_D for $Re_D \geq 2 \times 10^6$ - 3.0×10^6. This last flow regime is the so-called transcritical flow state, in which the mean drag coefficient takes a mean value of $C_D \approx 1.15$ which lies at a level of about 85% of its mean subcritical value.

The distributions of the fluctuation of the lift force, $\sqrt{(\overline{C_L'^2})}$, in Fig. 3b also display some interesting features. Firstly, the $\sqrt{(\overline{C_L'^2})}$ distributions show qualitatively similar trends over all four flow states as was found for C_D, hence high constant values in the

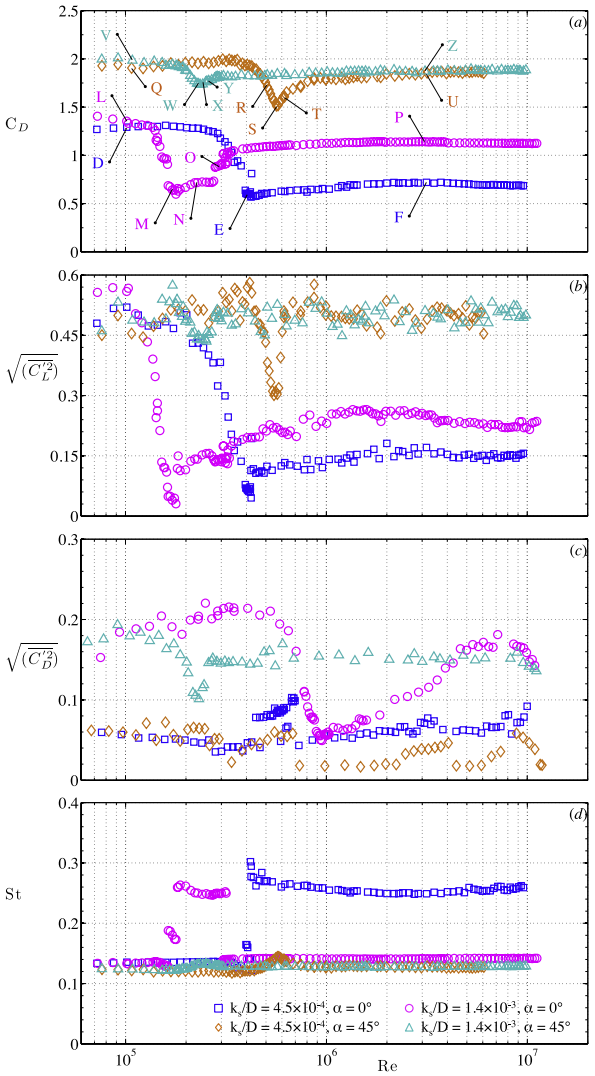

Fig. 5. Mean drag coefficient, fluctuations of the lift and drag coefficients, and Strouhal number as function of the Reynolds number for the two-dimensional square prism with rounded edges of $r/D = 0.16$ at angles of incidence of $\alpha = 0^\circ$ and 45°. □: $k_s/D = 4.5 \times 10^{-4}$, $\alpha = 0^\circ$ (*D*: subcritical, $Re_D = 1.0 \times 10^5$ - *E*: critical, $Re_D = 4.1 \times 10^5$ - *F*: supercritical, $Re_D = 3.2 \times 10^5$); △: $k_s/D = 4.5 \times 10^{-4}$, $\alpha = 45^\circ$ (*Q*: subcritical, $Re_D = 1.1 \times 10^5$ - *R*: critical, $Re_D = 5.1 \times 10^5$ - *S*: supercritical, $Re_D = 5.6 \times 10^5$ - *T*: upper transition, $Re_D = 6.0 \times 10^5$ - *U*: transcritical, $Re_D = 3.2 \times 10^6$); ∘: $k_s/D = 1.4 \times 10^{-3}$, $\alpha = 0^\circ$ (*L*: subcritical, $Re_D = 1.0 \times 10^5$ - *M*: critical, $Re_D = 1.7 \times 10^5$ - *N*: supercritical, $Re_D = 2.3 \times 10^5$ - *O*: upper transition, $Re_D = 2.9 \times 10^5$ - *P*: transcritical, $Re_D = 3.1 \times 10^6$); △: $k_s/D = 1.4 \times 10^{-3}$, $\alpha = 45^\circ$ (*V*: subcritical, $Re_D = 1.1 \times 10^5$ - *W*: critical, $Re_D = 2.4 \times 10^5$ - *X*: supercritical, $Re_D = 2.6 \times 10^5$ - *Y*: upper transition, $Re_D = 2.7 \times 10^5$ - *Z*: transcritical, $Re_D = 3.2 \times 10^6$).

subcritical flow state, a strong decrease in the critical flow state, constant low values for the supercritical flow state and an increase followed by nearly constant values in the upper transition and transcritical flow states, respectively. Secondly, the steep drops that occur in all four $C_D(Re_D)$-curves in the critical flow state in Fig. 3a are in the $\sqrt{(\overline{C_L'^2})}$ distributions either only very moderate or even non-existent at the same Reynolds numbers. The same applies to the somewhat weaker jumps upwards in the upper transition flow state for the two highest surface roughness values. Thirdly, although the values of $\sqrt{(\overline{C_L'^2})}$ nearly double within the upper transition, they only reach about half the amount of their subcritical values within the transcritical flow state ($\sqrt{(\overline{C_L'^2})} \approx 0.25$ in comparison to $\sqrt{(\overline{C_L'^2})} = 0.60$–$0.65$ for $Re_D \leq 1 \times 10^5$), hence their recovery is much lower than was found for C_D. Last, but not least, it is interesting to note that the curves for the smooth and slightly rough prisms lie on top of one another over a wide range of Reynolds numbers, the critical flow state being the only exception. Hence, an increase in marine growth height by a factor 100 on an initially smooth square prism has only a limited effect on the lift fluctuations. A similar observation can be made for both other $\sqrt{(\overline{C_L'^2})}$ distributions, for which even a much stronger overlapping is present in all flow states, in agreement with their corresponding $C_D(Re_D)$-curves.

The trends of the curves of the mean base pressure coefficient $C_{p,b}$ with Reynolds number, Fig. 4, closely follow the $C_D$distributions in Fig. 3a. This is not surprising, since for bluff body flows both coefficients are strongly coupled, as will be explained in detail in Section 5. High mean drag coefficient values of $C_D = 1.25$–1.4 in the subcritical flow state in Fig. 3a clearly correspond to large negative base pressure coefficients of $C_{p,b} = -0.95$ to -1.05 in Fig. 4. A strong increase in $C_{p,b}$ occurs for all curves in the subsequent critical flow state down to values as high as -0.65 ($k_s/D = 4.5 \times 10^{-6}$ and 4.5×10^{-4}) and -0.5 ($k_s/D = 1.0 \times 10^{-3}$ and 1.4×10^{-3}), in combination with clear steep jumps in $C_{p,b}$ at $Re_D = 5.4 \times 10^5$ and 6.4×10^5 for the smooth prism and at $Re_D = 3.8 \times 10^5$, 4.2×10^5 (not observed in the $C_D(Re_D)$ distribution) and 1.6×10^5 for the slightly rough and very rough prism, respectively. All curves show slight to moderate recoveries in $C_{p,b}$ either at the beginning of the supercritical flow state up to Reynolds numbers of 2–3 million or over the complete upper transition flow state. Surprisingly, the dependency of the mean base pressure coefficient on the height of the simulated hard marine fouling largely diminishes for $Re_D \geq 3 \times 10^6$.

4.1.2. Strouhal number

Fig. 3c shows the behaviour of the Strouhal number, which is based on the main vortex shedding frequency in the PSD of the lift force, with Reynolds number. The trends for the subcritical, critical and supercritical flow states are similar for the four studied prisms. A shift of these flow states towards lower Reynolds numbers with increasing k_s/D is observed in all four curves, whereas an increase of k_s/D beyond 1×10^{-3} has hardly any additional effect. Constant Strouhal numbers of $St_L = 0.14$ are present for all subcritical Reynolds numbers, whereas a slight decrease of about 5%–10% is observed at the beginning of the critical flow state. Within the critical flow states two kinds of behaviour of the Strouhal number with Reynolds number are found, depending on the value of k_s/D. For the smooth and rough prisms there exists a small range of Reynolds numbers in which two Strouhal numbers are present: $St_L = 0.13$ and 0.28 within $5.5 \times 10^5 \leq Re_D \leq 6.4 \times 10^5$ for the smooth prism and $St_L \approx 0.13$ and 0.26 within $1.6 \times 10^5 \leq Re_D \leq 1.9 \times 10^5$ for the rough prism. Since in both cases the lower Strouhal number is linked to the subcritical flow state and the higher one to the supercritical flow state, this means that for these critical Reynolds numbers the flow around the prism switches continuously back and forth between the subcritical and supercritical flow states, before settling at a constant supercritical Strouhal number of $St_L = 0.29$ ($k_s/D = 4.5 \times 10^{-6}$) and $St_L = 0.29$ ($k_s/D = 1.0 \times 10^{-3}$). The second possibility of the Strouhal-number behaviour in the critical flow state is observed for the curves belonging to the slightly rough and very rough prisms. Here, two subsequent jumps upward in the $St_L(Re_D)$-curves are seen to take place, first to an intermediate level of Strouhal numbers of 0.16 or 0.17–0.19 at $Re_D = 3.9 \times 10^5$ or 1.6×10^5, respectively, followed by a second jump at $Re_D = 4.2 \times 10^5$ towards $St_L = 0.3$ for the slightly rough prism and at $Re_D = 1.8 \times 10^5$ towards $St_L = 0.26$ for the very rough prism. The supercritical Strouhal numbers are then again characterised by a slight decrease at low supercritical Reynolds numbers. Whereas the $St_L(Re_D)$-curves belonging to the smooth and slightly rough prisms settle at constant plateaus of $St_L = 0.26$–0.27 which both prolong up to $Re_D = \mathcal{O}(10^7)$, the Strouhal numbers for the square prisms with $k_s/D \geq 1.0 \times 10^{-3}$ drop to values of 0.14, i.e. close to their subcritical levels, at those Reynolds numbers at which a jump in the corresponding C_D distributions takes place as well.

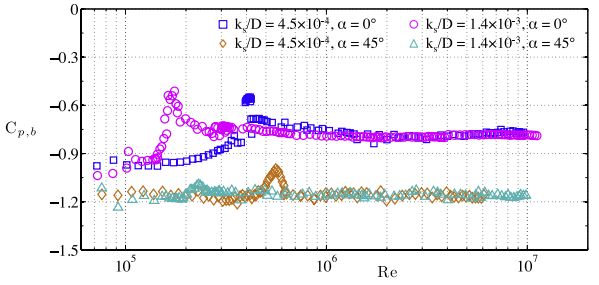

Fig. 6. Mean base pressure coefficient as function of the Reynolds number for the two-dimensional slightly rough ($k_s/D = 4.5 \times 10^{-4}$) and very rough ($k_s/D = 1.4 \times 10^{-3}$) prisms with rounded edges of $r/D = 0.16$ at both "symmetric" angles of incidence.

4.2. Variation in angle of incidence for two thicknesses of hard marine growth

For the slightly rough and vey rough prisms a comparison of the distributions of C_D, $\sqrt{(\overline{C_L'^2})}$, $\sqrt{(\overline{C_D'^2})}$, St_L and $C_{p,b}$ with Reynolds number between $\alpha = 0^{\circ}$ and 45° are presented in Figs. 5 and 6.

In general, a similar behaviour of the present data as described by Van Hinsberg et al. [47] for the smooth and rough square prisms with $r/D = 0.16$ is observed, namely drastic differences in the aerodynamics between the prisms at $\alpha = 0^{\circ}$ and at $\alpha = 45^{\circ}$. The general trends are a strong increase in mean drag, a decrease of the Strouhal number to a relatively constant subcritical level in combination with higher fluctuations of the lift force and higher mean base pressure coefficients. At 45° incidence angle all of these aerodynamic parameters furthermore show a large Reynolds-number independency and little variation with k_s/D throughout the investigated Reynolds-number range, with the exception of $\sqrt{(\overline{C_D'^2})}$ in case of the latter trend.

4.2.1. Mean and fluctuating aerodynamic loading

Fig. 5a shows the $C_D(Re_D)$-curves of the slightly rough and very rough square prisms for both "symmetric" angles of incidence. For both angles the trends mentioned above can clearly be recognised. A change from $\alpha = 0^{\circ}$–45° results for both values of k_s/D in an increase of C_D over the complete Reynolds-number range and a weaker dependency on the Reynolds number, in particular in the critical to upper transition flow stages.

The subcritical C_D-values increase by 45–50% up to values of 1.9–2.0 and a slight shift of the beginning of the critical flow state towards higher Reynolds numbers occurs, this shift being somewhat larger for the slightly rough prism. For $\alpha = 0^{\circ}$ the decrease in C_D in the critical flow state is more than 50% for both surface roughness values and both curves show a steep drop at the end of this flow state. On the contrary, at $\alpha = 45^{\circ}$ a steady decline (without any sudden drops) of the mean drag coefficient of "merely" 25% ($\Delta C_D = 0.5$) or 10% ($\Delta C_D \approx 0.2$) are obtained for both prisms. Nevertheless, the slope of drop of C_D in the critical flow state for the slightly rough square prism is found to be similar for both angles of incidence. A similar observation can be made when comparing the trends of the fluctuations of the lift force, $\sqrt{(\overline{C_L'^2})}$, in the same flow state in Fig. 5b. Whereas for the slightly rough prism at $\alpha = 0^{\circ}$ the supercritical flow state with low C_D values of 0.6–0.7 continues up to the highest investigated Reynolds number of $Re_D = 10$ million, this flow stage shrinks at $\alpha = 45^{\circ}$ to a single point with $C_D = 1.52$ at $Re_D = 5.7 \times 10^5$ and is followed by the appearances of the upper transition and transcritical flow stages. In these two flow states a recovery of the mean drag coefficient, followed by a plateau of constant C_D is observed. The supercritical flow state for the very rough prism at $\alpha = 45^{\circ}$ decreases as well in width and spans only a Reynolds-number range of roughly $\Delta Re_D = 3 \times 10^4$. As a result, the upper transition flow state starts for both angles of incidence at approximately equal Reynolds numbers. At $\alpha = 45^{\circ}$ both prisms possess roughly constant transcritical mean drag coefficients that are as high as 95% of their subcritical values.

The trends of the fluctuations of the lift force, $\sqrt{(\overline{C_L'^2})}$, and of the drag force $\sqrt{(\overline{C_D'^2})}$, in Fig. 5b and c shows completely different behaviours with k_s/D and α for $60{,}0000 \leq Re_D \leq 12$ million. The strong Reynolds-number dependency of $\sqrt{(\overline{C_L'^2})}$ for both prisms at $\alpha = 0^{\circ}$ in Fig. 5b diminishes for 45° angle of incidence. Both curves belonging to $\alpha = 45^{\circ}$ show approximately constant levels for $\sqrt{(\overline{C_L'^2})}$ of 0.51 ± 0.07. Whereas at $\alpha = 0^{\circ}$ a clear effect of increasing k_s/D is observed in all flow states, this influence has thus basically disappeared at $\alpha = 45^{\circ}$, with the exception of a small Reynolds-number range from the critical up to upper transition flow stages. In these flow states a small to moderate dip in both curves is seen to occur, which correlates with the decrease and subsequent increase in the corresponding curves of the mean drag coefficient in Fig. 5a.

The distributions of $\sqrt{(\overline{C_D'^2})}$ for the slightly rough prism at $\alpha = 0^{\circ}$ and 45° in Fig. 5c have fairly similar values. The curve for $\alpha = 0^{\circ}$ possesses a relatively large independency on the Reynolds number in the various flow states, slightly higher values of $\sqrt{(\overline{C_D'^2})} = 0.8$–$1.0$ are only observed at the beginning of the supercritical flow state between $Re_D = 4.5 \times 10^5$ and 7.0×10^5 and at the highest investigated Reynolds numbers of about 10 million. Somewhat larger variations in $\sqrt{(\overline{C_D'^2})}$with Re_D have been measured for 45° angle of incidence. Much higher values of $\sqrt{(\overline{C_D'^2})}$ are obtained for the very rough prism at both angles of incidence. The steep decrease in the $\sqrt{(\overline{C_D'^2})}$ (Re_D)-curve of about 75% in the critical flow state down to $\sqrt{(\overline{C_D'^2})} = 0.05$ for $5.9 \times 10^5 \leq Re_D \leq 9.5 \times 10^5$ and subsequent steady recovery in the upper transition flow state up to a subcritical level for $\alpha = 0^{\circ}$ has, at $\alpha = 45^{\circ}$, shifted towards lower Reynolds numbers and now corresponds with the slight dips in C_D and $\sqrt{(\overline{C_L'^2})}$ which take place between the critical and upper transition flow states. Interestingly, the drop in and subsequent recovery of $\sqrt{(\overline{C_D'^2})}$ in these flow states are both not as strong as observed for the wide dip at $\alpha = 0^{\circ}$, as a result of which transcritical values of only $\sqrt{(\overline{C_D'^2})} = 0.15$ are obtained at $\alpha = 45^{\circ}$, being about 20% lower than their subcritical values. In comparison to 0° angle of incidence, they remain at a constant level throughout the complete transcritical flow state though.

The distributions of the mean base pressure coefficient in Fig. 6 show two distinct levels, each of which related to one of both investigated angles of incidence and independent of the value of k_s/D. The trends in the various flow states are similar for all curves: constant low subcritical values of $C_{p,b} \approx$ -1.0 and -1.16 for $\alpha = 0^{\circ}$ and 45°, respectively, followed by a moderate to steep increase -

including a small jump in both curves for α = 0° - in the critical flow state up to values of $C_{p,b} = -0.55$ ($k_s/D = 4.5 \times 10^{-4}$) and −0.51 ($k_s/D = 1.4 \times 10^{-3}$) at α = 0°, and $C_{p,b} = -1.00$ ($k_s/D = 4.5 \times 10^{-4}$) and −1.09 ($k_s/D = 1.4 \times 10^{-3}$) at α = 45°. For both prisms at α = 0° a subsequent moderate decrease of the mean base pressure coefficient is observed, for the slightly rough prism within the supercritical flow state and for the very rough prism within the supercritical up to transcritical flow states. Interesting to note is, that, although different flow states are reached for $Re_D \geq 1.5$ million at 0° incidence angle, both curves lie perfectly well on top of each other at $C_{p,b} = -0.8$ up to Reynolds numbers of 10 million. In case of α = 45° this recovery of $C_{p,b}$ in the upper transition flow state leads to transcritical base pressure coefficients that are not only independent of both Re_D and k_s/D, but obtain subcritical values as well.

4.2.2. Strouhal number

Fig. 5d shows that only small differences in the subcritical and the transcritical Strouhal numbers are present between both incidence angles and that the values of St_L do not depend on k_s/D. For the prisms at α = 0° two subsequent upward jumps in the $St_L(Re_D)$-curves lead to large changes in St_L with Reynolds number in the critical flow state and in high constant Strouhal numbers of $St_L = 0.3$ (for $k_s/D = 4.5 \times 10^{-4}$) and 0.26 (for $k_s/D = 1.4 \times 10^{-3}$) in the supercritical flow state. For the very rough prism this

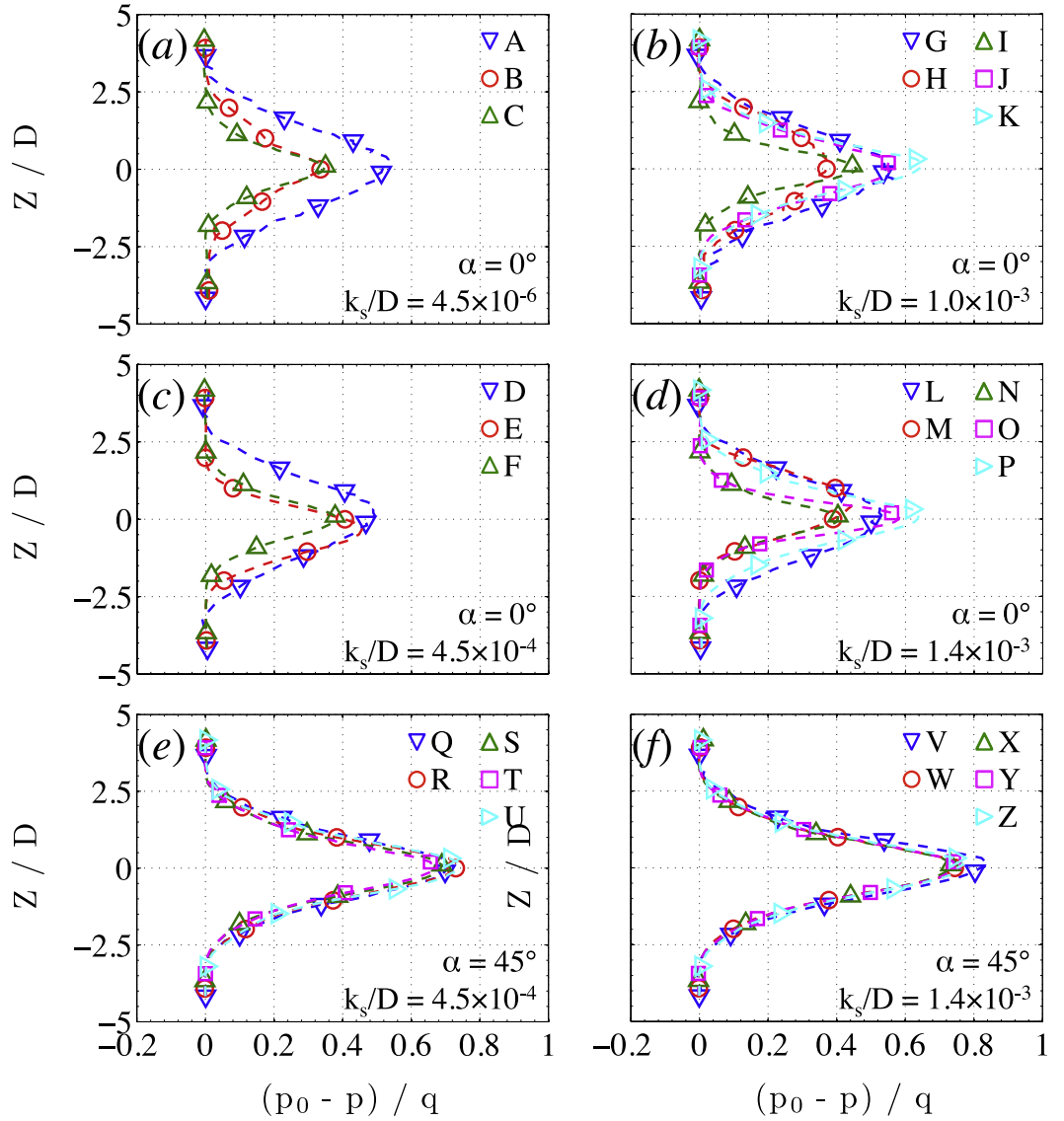

Fig. 7. Mean two-dimensional wake profiles belonging to the various Reynolds-number flow regimes of the two-dimensional square prism with $r/D = 0.16$. (*a*): $k_s/D = 4.5 \times 10^{-6}$, α = 0°; (*b*): $k_s/D = 1.0 \times 10^{-3}$, α = 0°; (*c*): $k_s/D = 4.5 \times 10^{-4}$, α = 0°; (*d*): $k_s/D = 1.4 \times 10^{-3}$, α = 0°; (*e*): $k_s/D = 4.5 \times 10^{-4}$, α = 45°; (*f*): $k_s/D = 1.4 \times 10^{-3}$, α = 45°. *Z* is the upwards-directed axis seen from the spanwise centre of the prism, p_0 the total pressure at the inlet, *p* the pitot pressure at vertical locations in the near wake and *q* the dynamic pressure at the inlet. The individual stages *A* to *Z* correspond to the stages in Fig. 3a and 5a. The pressure rake is positioned at mid-span location 6.25 prism widths behind the spanwise centre axis of the prism.

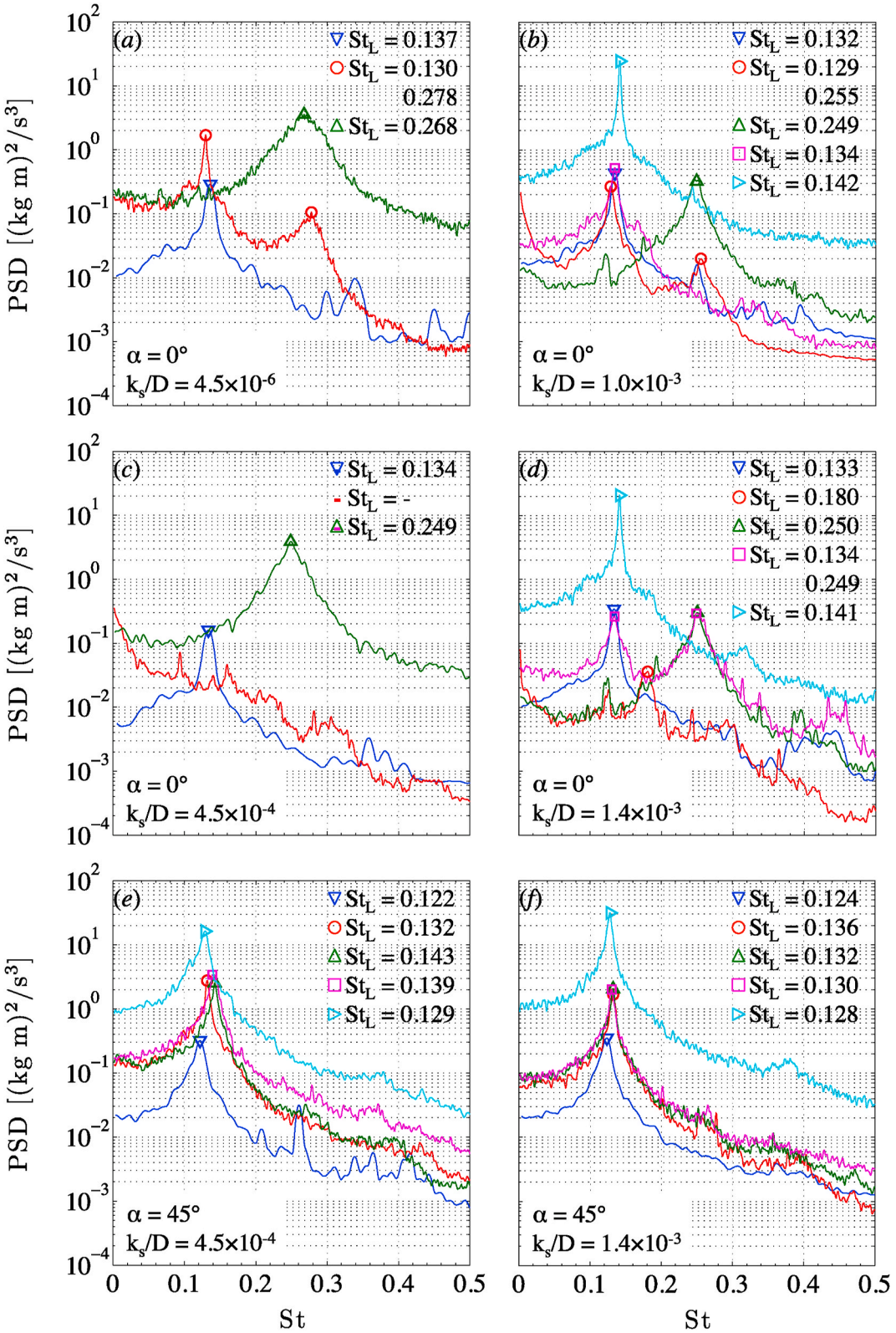

Fig. 8. Power spectral density of the unsteady lift forces for various Reynolds-number flow states of the two-dimensional square prism with $r/D = 0.16$. (*a*): $k_s/D = 4.5 \times 10^{-6}$, $\alpha = 0°$; (*b*): $k_s/D = 1.0 \times 10^{-3}$, $\alpha = 0°$; (*c*): $k_s/D = 4.5 \times 10^{-4}$, $\alpha = 0°$; (*d*): $k_s/D = 1.4 \times 10^{-3}$, $\alpha = 0°$; (*e*): $k_s/D = 4.5 \times 10^{-4}$, $\alpha = 45°$; (*f*): $k_s/D = 1.4 \times 10^{-3}$, $\alpha = 45°$. The individual curves correspond to the stages *A* to *R* in Fig. 3a, 5a and 7.

supercritical flow state is limited by a straight plunge in the Strouhal number at $Re_D = 3 \times 10^5$ within the upper transition flow state down to subcritical Strouhal-number values. In contrast, this remarkable behaviour of the Strouhal number for increasing Reynolds numbers is absent in both curves for $\alpha = 45°$. The only noticeable variation in St_L with Reynolds number is a small bump. This close to independent behaviour of the Strouhal number within the range of $Re_D = 8 \times 10^4$ - 10×10^6 is consistent with the results for the rough prism at 45° angle of incidence obtained by Van Hinsberg et al. [47]. It is, however, in contrast to the data of the smooth prism at $\alpha = 45°$, where the effects of the Reynolds number on the Strouhal number in the critical up to upper transition flow state were found to be more pronounced [47].

5. Discussion

In the preceding section it was shown that the thickness of the simulated hard marine fouling, the Reynolds number, and the angle of incidence of the prism all induce distinct and partly completely different effects on the fluctuating and mean loading on a square prism with rounded edges of $r/D = 0.16$. Larger surface roughness heights lead to a reduction of the widths of the subcritical up to upper transition flow states and a shift of their boundaries towards lower Reynolds numbers. On the contrary, in case of a change in angle of incidence from 0° to 45° only a decrease in the width of the supercritical flow state is observed. The lengths of the critical and upper transition flow states remain close to stable, whereas the subcritical flow state even expands in width. The mean drag coefficient, the fluctuations in lift and drag, the Strouhal number and the mean base pressure coefficient all become largely independent of the Reynolds number for $\alpha = 45°$ and this independency increases with increasing non-dimensional surface roughness height. This is in contrast to the curves of the same aerodynamic parameters at $\alpha = 0°$, for which a large variation in values with Reynolds number is obtained for all studied surface roughness heights. Interestingly, the subcritical values of C_D, $\sqrt{(\overline{C_L'^2})}$ and St_L in Fig. 3 and of $C_{p,b}$ in Fig. 4 belonging to the four investigated prisms at $\alpha = 0°$ are found to be close to independent of the value of k_s/D. The same behaviour is observed for the amount of decrease of C_D and $\sqrt{(\overline{C_L'^2})}$, as well as the amount of increase of St_L and $C_{p,b}$ throughout the critical flow state. This independency on the surface roughness therefore also results in similar values of these aerodynamic coefficients among the four prisms in the subsequent supercritical flow state. These behaviours of C_D, $\sqrt{(\overline{C_L'^2})}$, St_L and $C_{p,b}$, as well as the wake profile characteristics, with surface roughness height on one hand and with incidence angle on the other hand will be addressed in more detail hereafter.

5.1. Combined effects of increase in Reynolds number and simulated hard marine fouling thickness

The cause of the changes in the flow phenomena with increasing Reynolds number and surface roughness height at $\alpha = 0°$ can be found in the nature of both the boundary layer on the surface of the prism and of the free shear layers. In particular the locations of the transition from laminar to turbulent, taking place either on the surface of the prism or on the free shear layers, and the locations of the boundary layer separations from the surface play a very prominent role. In case of a reattachment of the free shear layers onto one or both side surfaces of the prism, the reattachment location(s), i.e. the length(s) of the separation bubble(s), and the secondary separation point(s) of the attached turbulent boundary layer are remarkable influencing parameters as well.

For subcritical Reynolds numbers the attached boundary layer on the surface of the smooth prism is laminar and separates at the forward directed rounded edges between the surfaces *I* and *II* and the surfaces *I* and *IV* of the prism at $\alpha = 0°$ (Fig. 2b). As a consequence, a strong deflection of the streamlines and a distinct spreading of the free shear layers in cross-flow direction occur. The transition from laminar to turbulent flow occurs for these low Reynolds numbers on both free shear layers in the (near) wake region and moves with increasing subcritical Reynolds number upstream along these free shear layers towards both trailing edges of the prism. Since both free shear layers are widely separated from each other, a wide near wake of 6 prism widths is still present at 5.75 prism widths downstream of the prism base as is shown by the curve *A* of the mean wake profiles in Fig. 7a.

In combination with a large suction pressure on the rear surface (Fig. 4), this leads to a high mean drag coefficient of $C_D \approx 1.3$ (Fig. 3a). Because of the large separation of the free shear layers, strong fluctuations of C_L are produced by the interaction of both shear layers in the near wake (Fig. 3b). The subcritical flow state is furthermore defined by a relatively narrow band frequency spectrum of the unsteady lift force (curve *A* for $Re_D = 1.2 \times 10^5$ in Fig. 8a) around the Strouhal number of about 0.14.

With increasing Reynolds number into the critical flow state the transition locations move further upstream along the free shear layers above both side surfaces *II* and *IV*, thereby inducing a weaker deflection of the streamlines, a lower lateral spacing of the separated shear layers, hence an increase of $C_{p,b}$, and thus a smaller wake width and a lowering of C_D, as is shown in Figs. 4 and 3a and exemplary for $Re_D = 6.1 \times 10^5$ by curve *B* in Fig. 7a, respectively. The steady approach of the free shear layers towards the leading edges of the prism with increasing critical Reynolds numbers and the resulting weaker interaction of both shear layers in the base region of the prism lead to a steep decrease of $\sqrt{(\overline{C_L'^2})}$. The power spectral density of the lift fluctuations at $Re_D = 6.1 \times 10^5$ (curve *B* in Fig. 8a) shows two clear peaks, the first one at $St_L = 0.130$ corresponding to the subcritical flow state, the second one at $St_L = 0.278$ belonging to the supercritical flow state. At this stage the laminar-turbulent transition is located above both side surfaces *II* and *IV* in the vicinity of the two leading edges. Above the two side faces the flow behaviour is therefore quite dynamic: either the turbulent free shear layers have enough energy to be able to reattach to the side surfaces of the prism, thereby forming a shallow recirculation region above both side surfaces, or the free shear layers remain separated up to the base region, as the energy of the flow is not sufficient enough to force a reattachment. In the former case a re-separation of the attached turbulent boundary layer occurs at the leeward-

directed edges of the prism, induced by the strong pressure increase inside of the surface boundary layer over these rounded edges. As has already been mentioned in section 4.1.2 the flow around the prism and thus the topology of the near wake switches at this critical Reynolds number continuously back and forth between both stages which correspond, according to the main peaks in the power spectral density curve *B* of the lift force in Fig. 8a, to the subcritical and supercritical flow states. Note that the presented mean surface pressure distributions and the mean wake profiles are obtained at the mid-span location of the prism only, hence the possible existence of a spanwise variation in the pressure field and thus a three-dimensional flow around the prism at certain Reynolds numbers within the critical flow state cannot be proven, but should, at the same time, not be excluded.

In the following supercritical flow state the transition locations on the laminar free shear layers have settled firmly above both side surfaces *II* and *IV* in the vicinity of the two leading edges, leading to a steady reattachment of the turbulent free shear layer and the presence of a shallow separation bubble on the upstream portions of the surfaces *II* and *IV* of the prism [55]. The separation of the turbulent boundary layer has shifted to its most downstream location on the rounded trailing edges of the prism. Compared to the laminar free shear layers in the subcritical flow state, the turbulent free shear layers that depart from these edges are formed relatively close together in the base region. Cao and Tamura [55], for example, showed that the recirculation region behind a prism with a square cross-section and rounded edges of $r/D = 0.167$ at a supercritical Reynolds number of 1×10^6 possesses both a much smaller length and width of, respectively, $L_f = 1.07$ and $d_w < D$ compared to their subcritical values ($L_f = 1.49$ and $d_w > D$) at $Re_D = 2.2 \times 10^4$. The location of the turbulent boundary layer separation on the rounded trailing edges and the resultant much smaller recirculation region lead to $C_{p,b}$-values that are less negative than for subcritical Reynolds numbers (Fig. 4). Because the parameter $\sqrt{(\overline{C_L'^2})}$ can be seen as a measure of the intensity of the vortex shedding process, it becomes clear that a decrease of the lift fluctuations by about 50% compared to the subcritical flow state in Fig. 3b is associated with a much weaker interaction of both turbulent free shear layers in the base region. In combination with the larger horizontal component of the negative pressure peak on the windward-directed rounded edges, the smaller suction pressure at the base of the prism, and the small wake width of less than 4 prism widths (curve *C* at $Re_D = 3.1 \times 10^6$ in Fig. 7a) low mean drag coefficients of $C_D = 0.6$ are obtained (Fig. 3a). Moreover, in comparison with the subcritical and critical flow states, a relatively broad main peak around $St_L = 0.27$ is present in the PSD of the lift force (Fig. 8a). The nearly constant plateaus of the

Table 2
Mean width Z/D and maximum total non-dimensional pressure loss $\Delta p_{max} = (p_0 - p)/q_\infty$ of the wake at 6.25 prism widths downstream of the spanwise centre axis of the smooth and slightly to very rough prisms at Reynolds numbers belonging to the various flow states.

α	k_s/D	Flow state	Re_D	Mean wake width Z/D	Maximum total non-dimensional pressure loss Δp_{max}
0°	4.5×10^{-6}	Subcritical	1.2×10^5	6.0	0.53
		Critical	6.1×10^5	5.5	0.34
		Supercritical	3.1×10^6	3.8	0.35
	4.5×10^{-4}	Subcritical	1.0×10^5	5.8	0.49
		Critical	4.1×10^5	3.9[a]	0.46
		Supercritical	3.2×10^6	4.0	0.38
	1.0×10^{-3}	Subcritical	1.1×10^5	6.2	0.53
		Critical	1.7×10^5	5.8	0.37
		Supercritical	2.3×10^5	3.8	0.46
		Upper transition	2.6×10^5	4.7	0.55
		Transcritical	3.2×10^6	5.1	0.65
	1.4×10^{-3}	Subcritical	1.0×10^5	6.0	0.53
		Critical	1.7×10^5	3.8[a]	0.44
		Supercritical	2.3×10^5	4.0	0.40
		Upper transition	2.9×10^5	4.0	0.58
		Transcritical	3.1×10^6	5.1	0.64
45°	4.5×10^{-4}	Subcritical	1.1×10^5	5.5	0.70
		Critical	5.1×10^5	5.5	0.73
		Supercritical	5.6×10^5	5.1	0.69
		Upper transition	6.0×10^5	5.1	0.66
		Transcritical	3.2×10^6	5.5	0.74
	1.4×10^{-3}	Subcritical	1.1×10^5	5.5	0.84
		Critical	2.4×10^5	5.3	0.75
		Supercritical	2.6×10^5	5.1	0.73
		Upper transition	2.7×10^5	5.3	0.74
		Transcritical	3.2×10^6	5.5	0.77

[a] asymmetric bistable flow state with one-sided separation bubble.

various aerodynamic coefficients up to supercritical Reynolds numbers of about 12 million imply that, with increasing Reynolds number, hardly any changes occur in the locations of the transition points, of the main laminar and secondary turbulent boundary layer separation points, and of the turbulent free shear layer reattachment points. The same applies to the flow field around the prism and the topology of the near wake behind the prism.

From systematic experimental studies on the influence of surface roughness on the wind loading experienced by "infinite" circular cylinders in cross-flow it is known that an increasing surface roughness height induces a reduction of the widths of the subcritical up to upper transition flow states, as a result of which the beginning of the transcritical flow state appears at significantly lower Reynolds numbers, e.g. Ref. [20]. A similar behaviour could be observed in the current data in Figs. 3 and 4 for the studied square prism with rounded edges. For both cross-sectional shapes this flow behaviour is caused by a similar underlying physical mechanism, since they both possess a rounded and continuous cross-sectional shape. A larger surface roughness induces a more rapid growth and amplification of the boundary layer instabilities, which then trigger the transition from laminar to turbulent flow in the attached boundary layer at an earlier circumferential location on the wall surface of the circular cylinder or rounded prism. Compared to their smooth counterparts this earlier transition then again forces a separation of the turbulent boundary layer from the rougher surface at lower Reynolds numbers. The boundaries between the various flow states thus shift to lower Reynolds numbers and the range of Reynolds numbers each one of them spans reduces with higher roughness. Furthermore, the shear layers that depart from the secondary separation locations are in this case turbulent as well.

The data for C_D, $\sqrt{(\overline{C_L'^2})}$, St_L, and $C_{p,b}$ in Figs. 3 and 4 show that for the current square prisms neither their actual subcritical and supercritical values nor their strong changes in the critical flow state are affected by the simulated hard marine growth. A similar behaviour can be observed for the near wake, when comparing the shapes of the mean wake profiles of the four prisms for each single

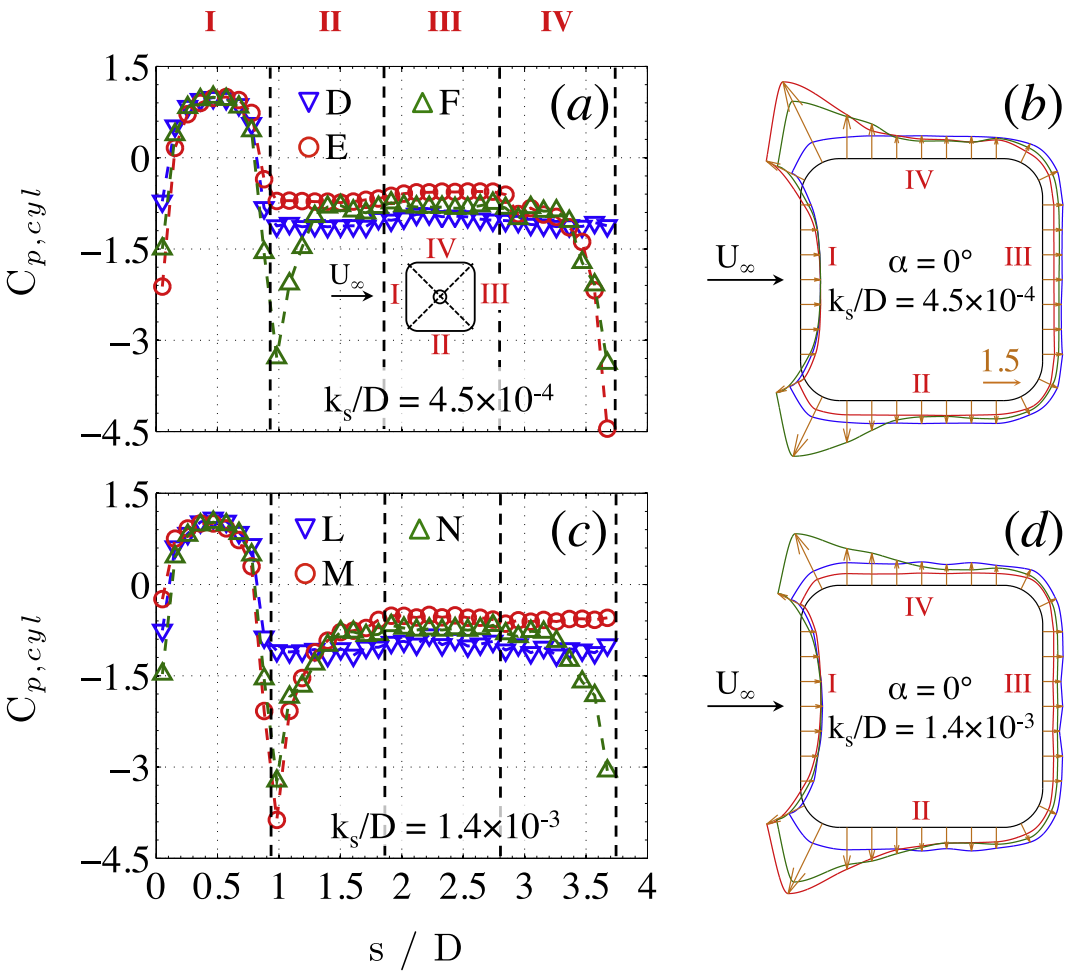

Fig. 9. Mean two-dimensional circumferential surface pressure distributions at mid-span of the 2D slightly rough and very rough square prisms with $r/D = 0.16$ at $\alpha = 0^\circ$. (*a*) and (*b*): $k_s/D = 4.5 \times 10^{-4}$ (*D*: subcritical, $Re_D = 1.0 \times 10^5$ - *E*: critical, $Re_D = 4.1 \times 10^5$ - *F*: supercritical, $Re_D = 3.2 \times 10^6$); (*c*) and (*d*): $k_s/D = 1.4 \times 10^{-3}$ (*L*: subcritical, $Re_D = 1.0 \times 10^5$ - *M*: critical, $Re_D = 1.7 \times 10^5$ - *N*: supercritical, $Re_D = 2.3 \times 10^5$). The letters *D* to *F* and *L* to *N* correspond to those points marked in Fig. 3a.

flow state at $\alpha = 0^\circ$ in Fig. 7a to d, as well as the associated non-dimensional wake widths Z/D and the maximum total non-dimensional pressure losses Δp listed in Table 2.

The independency of the subcritical aerodynamic coefficients on k_s/D is well known from the many experimental and numerical studies on the flow around smooth and (slightly) rough 2D circular cylinders [20,23,24,26,27,37,56–58]. It results from the fact that, at subcritical Reynolds numbers, the laminar boundary layer on those cylinders has a large thickness with respect to the height of the surface roughness. Its laminarity is therefore relatively unaffected by increasing surface roughness up to separation, as a result of which the roughness has little to no influence on both the mean and fluctuating subcritical loading experienced by circular cylinders and on the flow topology in their near wakes. The present subcritical aerodynamic results of the rounded square prisms suggest that for elements with this specific cross-sectional shape the laminar surface boundary layer behaves in a similar way.

Fage [19], Achenbach [20], Okajima and Nakamura [59] and Adachi [29] reported that for "infinite" smooth and (slightly) rough circular cylinders in cross-flow the variation of C_D, $C_{p,b}$, and St with Reynolds number in the critical and supercritical flow regimes

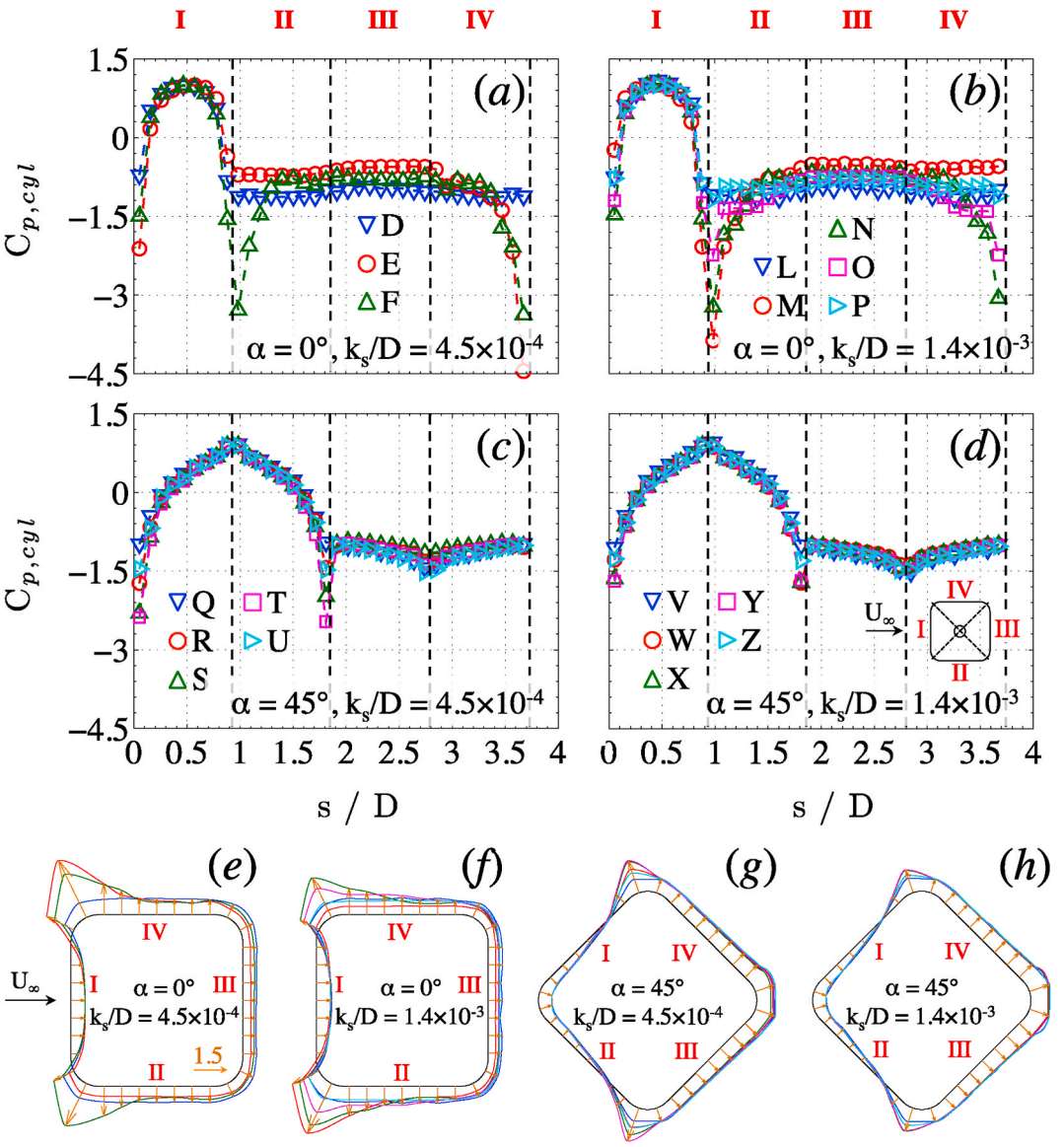

Fig. 10. Mean two-dimensional circumferential surface pressure distributions at mid-span of the two-dimensional slightly rough and very rough square prisms with $r/D = 0.16$ at $\alpha = 0^\circ$ and 45°. (*a*) and (*e*): $k_s/D = 4.5 \times 10^{-4}$, $\alpha = 0^\circ$ (*D*: subcritical, $Re_D = 1.0 \times 10^5$ - *E*: critical, $Re_D = 4.1 \times 10^5$ - *F*: supercritical, $Re_D = 3.2 \times 10^6$); (*b*) and (*f*): $k_s/D = 1.4 \times 10^{-3}$, $\alpha = 0^\circ$ (*L*: subcritical, $Re_D = 1.0 \times 10^5$ - *M*: critical, $Re_D = 1.7 \times 10^5$ - *N*: supercritical, $Re_D = 2.3 \times 10^5$ - *O*: upper transition, $Re_D = 2.9 \times 10^5$ - *P*: transcritical, $Re_D = 3.1 \times 10^6$); (*c*) and (*g*): $k_s/D = 4.5 \times 10^{-4}$, $\alpha = 45^\circ$ (*Q*: subcritical, $Re_D = 1.1 \times 10^5$ - *R*: critical, $Re_D = 5.1 \times 10^5$ - *S*: supercritical, $Re_D = 5.6 \times 10^5$ - *T*: upper transition, $Re_D = 6.0 \times 10^5$ - *U*: transcritical, $Re_D = 3.2 \times 10^6$); (*d*) and (*h*): $k_s/D = 1.4 \times 10^{-3}$, $\alpha = 45^\circ$ (*V*: subcritical, $Re_D = 1.1 \times 10^5$ - *W*: critical, $Re_D = 2.4 \times 10^5$ - *X*: supercritical, $Re_D = 2.6 \times 10^5$ - *Y*: upper transition, $Re_D = 2.7 \times 10^5$ - *Z*: transcritical, $Re_D = 3.2 \times 10^6$). The letters correspond to those points marked in Fig. 5a.

show a relatively large independency on the surface roughness height if k_s/D is smaller than 5×10^{-4}. Above this limiting value a considerable weakening of the abrupt changes of all three parameters in the critical flow state, hence a flattening of the curves with Reynolds number, takes place. As a result the critical Reynolds number at which $C_{D,min}$, $C_{p,b,min}$, and St_{max} occur, becomes smaller and the corresponding minimum values for C_D and $C_{p,b}$ increase, whereas St_{max} decreases. In the supercritical flow regime higher mean drag forces are therefore induced on the circular cylinder [19,20,27,29,37,59]. Figs. 3, 4, 7 and 8 and Table 2 clearly show that for the current 2D square prisms with $r/D = 0.16$ the critical and supercritical values of C_D, $\sqrt{(\overline{C_L'^2})}$, St_L, $C_{p,b}$, Z/D, and Δp are barely affected by an increase of k_s/D up to a value of at least 1.4×10^{-3}. It can be argued that this larger range of k_s/D is connected with the relatively low radius of curvature of the edges of the prisms and the resultant behaviour of the free shear layers and - in case of their reattachment on the side surfaces - of the attached turbulent boundary layer and the secondary separation at the trailing edges of these side surfaces. Fig. 9a and b and Fig. 9c and d shows the distributions of the mean surface pressure coefficients at the mid-sections of the slightly rough and very rough prisms, respectively, for three exemplary Reynolds numbers of the sub-to supercritical flow states.

Despite the differences in Reynolds number owing to the shifts of the flow states towards lower Reynolds numbers and their reduction in width with increasing roughness height, the mean surface pressure distributions of both prisms are remarkably similar. This accounts both for the shape(s) and maximum value(s) of one or both negative pressure peak(s) at $s/D = 0.98$ (i.e. on the rounded edge between the surfaces *I* and *II*) and $s/D = 3.67$ (i.e. on the rounded edge between the surfaces *I* and *IV*), associated with the formation of a separation bubble on the side surface(s) *II* and/or *IV*, respectively, in the critical and supercritical flow states, and for the height of the plateaus of C_p in the base region of the prisms. As this implies a nearly independent behaviour of the locations of the transition, separation, and reattachment points on the prism surface within each of these three flow states, it is not surprising that the mean drag coefficient, the lift fluctuations and the mean base pressure coefficient for each flow state in Figs. 3 and 4 all show a similar behaviour with surface roughness height as well. The same is true for the Strouhal number (Figs. 3c and 8) and the mean shape, the maximum total non-dimensional pressure loss and the width of the wake profile behind the prisms (Fig. 7 and Table 2). Interesting to note is that the one-sided reattachment of the free shear layer on the side surface *IV* ($k_s/D = 4.5 \times 10^{-4}$) or *II* ($k_s/D = 1.4 \times 10^{-3}$) in the critical flow state is still clearly visible in the asymmetric wake profiles. The wake profiles *E* and *M* both consist of a subcritical branch which is located at that side at which no reattachment has occurred yet (Fig. 9b and d), and of a supercritical branch at the opposite side, i.e. the upper and lower half of the curve in Fig. 7b and d, respectively.

Whereas an increase of the surface roughness height on the initially smooth prism by a factor 100 up to $k_s/D = 4.5 \times 10^{-4}$ only induced a shift of the first three flow states towards slightly lower Reynolds numbers, its further increase by only a factor of two up to $k_s/D = 1.0 \times 10^{-3}$ led to the sudden appearance of both the upper transition and the transcritical flow states for $Re_D \geq 2.6 \times 10^5$. An additional increase by 40% up to the largest studied surface roughness height of $k_s/D = 1.4 \times 10^{-3}$ then again had little to no additional influence on the aerodynamic behaviour of the very rough prism, as could be extracted from the data in Figs. 3, 4, 7 and 8. Achenbach [23] found in his experimental study on the loading on 2D smooth and rough circular cylinders a similar behaviour. He related this independency on surface roughness to the fact that at very high roughness values the tops of the roughness elements are located outside of the surface boundary layer and therefore generate no additional disturbing effect.

The appearance of the upper transition and transcritical flow states for the rough and very rough prisms is associated with a movement further upstream of the boundary layer transition points and a steady reduction in size of the separation bubbles on both side surfaces with increasing Reynolds number. The former results from the increased ratio of the height of the surface roughness to the boundary layer thickness. The tops of the roughness elements protrude into regions of higher velocity inside the boundary layer, thereby inducing an even more rapid growth and amplification of the instabilities in the surface boundary layer, hence disturbing its laminarity, and thus triggering its transition to turbulent flow already at a very early stage. Whereas the primary separation points remain situated at the windward rounded edges of the prism because of their low radius of curvature, the reattachment locations of the turbulent free shear layers on the side surfaces *II* and *IV* move, with increasing Reynolds number within the upper transition flow state, further upstream in the direction of the primary separation points. The mean surface pressure distributions for the very rough prism, presented in Fig. 10b and f, show that at a supercritical Reynolds number of $Re_D = 2.3 \times 10^5$ (curve *N*) the reattachment points are located at $s/D = 1.50$ and 3.16 (i.e. at about 60% of the side surface length), whereas they have wandered upstream along both side surfaces to $s/D = 1.40$ and 3.26 (i.e. at about 50% of the side surface length) at a somewhat larger Reynolds number of 2.9×10^5 in the upper transition flow state (curve *O*).

Based on the reduction of the height of the negative pressure peaks at $s/D = 0.98$ and 3.67 it can furthermore be stated, that with increasing Reynolds number the strength of the vortex captured inside each separation bubble reduces as well. Moreover, the secondary separation points move upstream along the leeward rounded edges of the prism. Because of the simultaneous occurrence of all of these phenomena, the distance in cross-flow direction between both turbulent free shear layers which depart from the secondary separation points increases again. As a consequence, not only the near wake widens (curves *J* and *O* in Fig. 7b and d, respectively, and Table 2) and the negative base pressure coefficient decreases again (Fig. 4), which, in combination with a smaller horizontal component of the negative pressure peak on the windward-directed rounded edges, leads to an increase of C_D (Fig. 3a), but also a stronger interaction of both free shear layers in the base region behind the prism occurs which produces larger fluctuations in the lift force (Fig. 3b).

Finally, at the end of the upper transition flow state, the separation bubbles disappear completely and the transcritical flow state is reached. The absence of the separation bubbles is confirmed by the mean surface pressure distribution for $Re_D = 3.1$ million (curve *P*) in Fig. 10b and f in which no negative pressure coefficient peaks at $s/D = 0.98$ and 3.67 are present anymore. In fact, this mean surface pressure distribution resembles the one obtained at subcritical Reynolds numbers, hence a separation of the - in the transcritical flow state much thinner and turbulent - boundary layer at both windward rounded edges, without subsequent reattachment of the free shear

layers and secondary separation of the attached turbulent boundary layer at the leeward rounded edges. This explains why the transcritical mean drag coefficients (Fig. 3a) and transcritical Strouhal numbers (Fig. 3c) both obtain (nearly) subcritical values. The same applies to the mean wake profiles K and P in Fig. 7b and d, respectively. Although the frequencies with which the vortices are shed in the base region for transcritical Reynolds numbers are equal to those obtained in the subcritical flow state, the transcritical values for $\sqrt{(\overline{C_L'^2})}$ in Fig. 3b suggest that the intensities of these vortices are less than half of their subcritical counterparts.

5.2. Combined effects of increase in Reynolds number and angle of incidence

The distributions of the mean surface pressure coefficients of the slightly and very rough prisms at $\alpha = 0^\circ$ and 45° are presented in Fig. 10 for Reynolds numbers belonging to the various flow states. Whereas for both prisms at 0° angle of incidence (Fig. 10a, b, 10e and 10f) very distinct changes in the pressure distributions with increasing Reynolds number are observed, as has been described in the previous section, only slight changes are seen to take place in the pressure coefficient peaks at $s/D = 0.98$ and 3.67 and in the base pressures for $\alpha = 45^\circ$ (Fig. 10c, d, 10g and 10h). Independent of the Reynolds number and surface roughness height the attached laminar boundary layer on the surfaces *I* and *II* of the prisms at $\alpha = 45^\circ$ separates at both shoulders between the surfaces *II* and *III* and between *I* and *IV*. The appearance of a negative pressure peak on the windward-directed rounded upper and lower edges for critical up to transcritical Reynolds numbers in Fig. 10c and d implies a reattachment of the separated free shear layers directly upon separation, hence a separation bubble is formed at this angular configuration as well. Since the pressure peaks are sharp and narrow it is assumed that these separation bubbles are even smaller than those found for both prisms at 0° angle of incidence; however, the spatial resolution of the surface pressure taps of $s/D = 0.103$–0.105 is not yet fine enough to resolve the exact locations of both separation bubbles on the surface. The reattachment of the turbulent free shear layers is then again followed almost immediately by a secondary separation of the turbulent boundary layers downstream of both shoulders at the leading edges of both leeward surfaces *III* and *IV*. The resultant larger separation in cross-flow direction between both free shear layers compared with $\alpha = 0^\circ$ leads for both prisms at all Reynolds numbers to a wider near wake of $Z/D = 5.1$–5.5 (Table 2) with a much larger maximum total non-dimensional pressure loss Δp (Fig. 7e and f). The formation of the vortices in the near wake region takes place close to the base of the prism, thereby inducing mean pressure coefficient values of $C_{p,b} = -1.0$ to -1.2 at the base of the prism [51,60], leading to high mean drag coefficients of $1.5 \leq C_D \leq 2.0$ (Fig. 5a). The lift fluctuations and the Strouhal number are affected by the larger lateral spacing of both free shear layers as well. The values of both parameters at $\alpha = 45^\circ$ lie on a similar level as obtained for subcritical Reynolds numbers at $\alpha = 0^\circ$, hence low Strouhal numbers and high fluctuations of C_L, the latter produced by large interactions of both shear layers in the base region behind the prism (Fig. 5b and d). Similar trends have been described by Van Hinsberg et al. [47] for their slightly rough counterparts, whereas larger variations of all aerodynamic parameters with Reynolds number were found for the smooth prism at $\alpha = 45^\circ$. The level of the fluctuations of the drag coefficient, being a measure for the intensity in flow direction of the shedding process, seems to be relatively unaffected by the change in angle of incidence though (Fig. 5c).

The small variations in the mean surface pressure distributions - in particular the values of the negative pressure coefficient peaks and the pressures at the base of the prism - with Reynolds number at $\alpha = 45^\circ$ are most probably caused by the minor movements of the transition points, the main separation locations, and the reattachment and secondary separation points, hence the widths of the recirculation bubbles, along the prism surface. Fig. 10 furthermore shows that a larger surface roughness induces a decrease in the C_p-variation with Reynolds number. Both of these phenomena are clearly mirrored in the behaviours of the various aerodynamic parameters and of the mean wake profiles with Reynolds number in Figs. 5–8 and in Table 2.

6. Conclusions

The behaviour of the mean drag coefficient C_D, the lift and drag fluctuations $\sqrt{(\overline{C_L'^2})}$ and $\sqrt{(\overline{C_D'^2})}$, the Strouhal number St_L, the mean base pressure $C_{p,b}$, the mean surface pressure distribution over the mid-span cross-section of the prism, and the mean wake profile was examined for the two-dimensional ("infinite") square prism with non-dimensional rounded edges of $r/D = 0.16$ in cross-flow, with the main focus on the effects of Reynolds number and the thickness of the simulated hard marine fouling on the prism. Wind tunnel experiments were conducted at Reynolds numbers between 60,000 and 12 million with prisms having different values of non-dimensional surface roughness: $k_s/D = 4.5 \times 10^{-6}$ (smooth), $k_s/D = 4.5 \times 10^{-4}$ (slightly rough), $k_s/D = 1.0 \times 10^{-3}$ (rough) and $k_s/D = 1.4 \times 10^{-3}$ (very rough). Both "symmetric" angles of incidence, $\alpha = 0^\circ$ or 45°, were studied. The main conclusions can be summarised as follows:

1. At 0° angle of incidence the surface roughness height has a very distinct influence on the behaviour of all investigated aerodynamic parameters with Reynolds number up to about $k_s/D \approx 1 \times 10^{-3}$, whereas a further increase in surface roughness beyond this value induces barely any additional effects. An increase in k_s/D leads to a reduction of the widths of the subcritical, critical and - for $k_s/D \geq 1 \times 10^{-3}$ - the supercritical and upper transition flow states and a shift of the borders of these flow states towards lower Reynolds numbers. In contrast to circular cylinder flows, the roughness height itself has barely any effect on the absolute values of the aerodynamic parameters for sub-to supercritical Reynolds numbers. For the smooth and slightly rough prisms the supercritical flow state with low values of C_D and $\sqrt{(\overline{C_L'^2})}$, and high Strouhal numbers is present up to $Re_D = 12$ million. In contrast, high surface roughness values of $k_s/D \geq 1 \times 10^{-3}$ induce a limitation of the supercritical flow state and the appearance of the upper transition

and the transcritical flow states. This results, for Reynolds numbers larger than 5×10^5 - 6×10^5, in a strong increase in mean drag and a decrease of the vortex shedding frequency, both to subcritical values. Moreover, the values of the fluctuations in lift, being a measure for the intensity of the shedding process, are twice as high as for the smooth and slightly rough square prism.

2. The values of C_D, $\sqrt{(\overline{C_L'^2})}$, St_L, and $C_{p,b}$ are strong functions of the angle of incidence as well. A change in α from 0° to 45° induces the following general trends: a strong increase in mean drag, a decease of the Strouhal number and of the mean base pressure coefficient, and an increase in the lift fluctuations to similar levels as are obtained for the subcritical Reynolds numbers at $\alpha = 0°$. All aerodynamic parameters furthermore show a large Reynolds-number independency and little variation with k_s/D throughout the studied Reynolds-number range. This independency on Re_D increases even further with increasing non-dimensional surface roughness height. For the slightly rough up to very rough square prisms the supercritical flow state has shrunk to a single point and is followed by the appearances of the upper transition and transcritical flow stages.
3. The behaviour of C_D, $\sqrt{(\overline{C_L'^2})}$, St_L, and $C_{p,b}$ with Re_D at $\alpha = 0°$, and to some extend also at 45°, are caused by simultaneous changes in the locations of the transition points either on the free shear layers or on the prism surface and of the locations of the boundary layer separation from the surface. Moreover, for critical up to transcritical Reynolds numbers, the reattachment of the turbulent free shear layers and the secondary turbulent boundary layer separation from the surface further downstream play a distinct role as well. Higher values of k_s/D trigger the transition and separation at lower Reynolds numbers, thus shifting the boundaries between the various flow states to lower Reynolds numbers and reducing their widths. The mean surface pressure distributions at both angles of incidence are nearly independent on k_s/D, which explains the independency of the absolute values of the aerodynamic parameters and of the wake profiles on k_s/D for sub-to supercritical Reynolds numbers at $\alpha = 0°$.

All in all, the present results show that an increase in hard marine growth on the outer surfaces of an initially smooth submerged structural element with a square cross-section and rounded edges of $r/D = 0.16$ by a factor of at least 200 induces high mean drag forces at realistic Reynolds numbers of $\mathcal{O}(10^6)$–$\mathcal{O}(10^7)$. The added surface roughness furthermore affects the mechanism of vortex formation, thereby increasing both the vortex strength and their spanwise coherence. Those give rise to even higher periodic lift forces at vortex shedding frequencies that are roughly 50% lower than found for smooth or slightly rough prismatic elements. Similar observations can be made for a change in angle of incidence from 0° to 45°. Both phenomena suggest an increase of the risk of possible resonances between the vortex-induced vibrations of the submerged foundation and other (rotating) parts of offshore wind turbines and thus of possible (critical) damage to the wind turbine.

Declaration of competing interest

The authors declare that they have no known competing financial interests or personal relationships that could have appeared to influence the work reported in this paper.

Acknowledgments

This research did not receive any specific grant from funding agencies in the public, commercial, or not-for-profit sectors. Technical assistance of Markus Löhr and Karsten Steiner of DNW (German Dutch Wind Tunnels) is gratefully acknowledged. Systemhaus Technik and Deharde are recognised for the construction and manufacturing of the wind tunnel models, respectively. Finally, the author would like to thank the reviewers for their fruitful comments and suggestions.

References

[1] The European Commission. A Clean Planet for all: a European strategic long-term vision for a prosperous, modern, competitive and climate neutral economy. 2018 [cited 01 April 2020].
[2] The European Commission. In-depth analysis in support of the commission communication com(2018) 773. A Clean Planet for all: a European strategic long-term vision for a prosperous, modern, competitive and climate neutral economy. 2018 [cited 01 April 2020].
[3] Hansen AD, Hansen LH. Wind turbine concept market penetration over 10 years (1995 - 2004). Wind Energy 2007;10(1):81–97.
[4] Morthorst PE, Kitzing L. Economics of building and operating offshore wind farms. In: Ng C, Ran L, editors. Offshore wind farms. Woodhead Publishing; 2016. p. 9–27.
[5] Forteath GNR, Picken GB, Ralph R, Williams J. Marine growth studies on the North sea oil platform montrose alpha. Mar Ecol Prog Ser 1982;8:61–8.
[6] Langhamer O, Wilhelmsson D, Engström J. Artificial reef effect and fouling impacts on offshore wave power foundations and buoys - a pilot study. Estuar, Coast and Shelf Sci 2009;82:426–32.
[7] Kerckhof F, Rumes B, Jacques T, Degraer S, Norro A. Early development of the subtidal marine biofouling on a concrete offshore windmill foundation on the Thornton Bank (southern North Sea): first monitoring results, I. J. Soc. for Underw. Technol. 2010;29(3):137–49.
[8] Fitridge I, Dempster T, Guenther J, de Nys R. The impact and control of biofouling in marine aquaculture: a review. Biofouling 2012;28(7):649–69.
[9] Jusoh I, Wolfram J. Effects of marine growth and hydrodynamic loading on offshore structures. J. Mek. 1996;1(1):77–98.
[10] Yang S-H, Ringsberg J, Johnson E. The influence of biofouling on power capture and the fatigue life of mooring lines and power cables used in wave energy converters. In: Proc. Of the 2nd int. Conf. Lisbon, Portugal: on Renew. Energies Offshore; 2016.
[11] Spraul C, Pham H-D, Arnal V, Reynaud M. Effect of marine growth on floating wind turbines mooring lines responses. In: Proc. Of the 23ème congrès français de Mécanique; 2017. Lille, France.
[12] Wolfram J. The effect of marine growth on vortex shedding and fatigue life of tubular members: results from a case study. In: Proc. Of the 1st int. Offshore and polar eng. Conf.; 1991. Edinburgh, United Kingdom.
[13] Olsen SM, Pedersen LT, Laursen MH, Kiil S, Dam-Johansen K. Enzyme-based antifouling coatings: a review. Biofouling 2007;23(5–6):369–83.
[14] Magin CM, Cooper SP, Brennan AB. Non-toxic antifouling strategies. Mater Today 2010;13(4):36–44.

[15] Schoefs F, Boukinda M. Modelling of marine growth effects on offshore structures loading using kinematics field of water particle. In: Proc. Of the 14th int. Offshore and polar eng. Conf. And exhib. Toulon, France; 2004.
[16] Shi W, Park H-C, Baek J-H, Kim C-W, Kim Y-C, Shin H-K. Study on the marine growth effect on the dynamic response of offshore wind turbines. Int J Precis Eng Manuf 2012;13(7):1167–76.
[17] Wright CS, Murphy J, Pakrashi V. The dynamic effects of marine growth on a tension moored floating wind turbine. In: Proc. Of the 2nd int. Conf. On renew. Lisbon, Portugal: Energies Offshore; 2016.
[18] Henry P-Y, Nedrebø EL, Myhaug D. Visualisation of the effect of different types of marine growth on cylinders' wake structure in low Re steady flow. Ocean Eng 2016;115:182–8.
[19] Fage A, Warsap JH. The effects of turbulence and surface roughness on the drag of a circular cylinder. Tech. Rep. 1283. Aero. Res. Comm. Rep. and Memo.; 1929.
[20] Achenbach E. Influence of surface roughness on the cross-flow around a circular cylinder. J Fluid Mech 1971;46:321–35.
[21] Batham JP. Pressure distributions on circular cylinders at critical Reynolds numbers. J Fluid Mech 1973;57:209–28.
[22] Szechenyi E. Supercritical Reynolds number simulation for two-dimensional flow over circular cylinders. J Fluid Mech 1975;70:529–42.
[23] Achenbach E. The effect of surface roughness on the heat transfer from a circular cylinder to the cross flow of air. J. of Heat Mass Transf. 1977;20:359–69.
[24] Güven O, Farell C, Patel VC. Surface-roughness effects on the mean flow past circular cylinders. J Fluid Mech 1980;98:673–701.
[25] Nakamura Y, Tomonari Y. The effects of surface roughness on the flow past circular cylinders at high Reynolds numbers. J Fluid Mech 1982;123:363–78.
[26] Niemann HJ, Hölscher N. A review of recent experiments on the flow past circular cylinders. J Wind Eng Ind Aerod 1990;33:197–209.
[27] Zdravkovich MM. Conceptual overview of laminar and turbulent flows past smooth and rough circular cylinders. J Wind Eng Ind Aerod 1990;33:53–62.
[28] Bearman PW, Harvey JK. Control of circular cylinder flow by the use of dimples. AIAA Paper 1993-1753; 1993.
[29] Adachi T. Effects of surface roughness on the universal Strouhal number over the wide Reynolds number range. J Wind Eng Ind Aerod 1997;69–71:399–412.
[30] Yamagishi Y, Oki M. Effect of groove shape on flow characteristics around a circular cylinder with grooves. J Vis 2004;7:209–16.
[31] Yamagishi Y, Oki M. Effect of the number of grooves on flow characteristics around a circular cylinder with triangular grooves. J Vis 2005;8:57–64.
[32] Yamagishi Y, Oki M. Numerical simulation of flow around a circular cylinder with curved sectional grooves. J Vis 2007;10:179–86.
[33] Achenbach E, Heinecke E. On vortex shedding from smooth and rough cylinders in the range of Reynolds numbers $6x10_3$ to $5x10^{\circ}$. J Fluid Mech 1981;109:239–51.
[34] Ribeiro JLD. Effects of surface roughness on the two-dimensional flow past circular cylinders I: mean forces and pressures. J Wind Eng Ind Aerod 1991;37:299–309.
[35] Behara S, Mittal S. Transition of the boundary layer on a circular cylinder in the presence of a trip. J Fluid Struct 2011;27:702–15.
[36] Schewe G. Sensitivity of transition phenomena to small perturbations in flow around a circular cylinder. J Fluid Mech 1986;172:33–46.
[37] van Hinsberg NP. The Reynolds number dependency of the steady and unsteady loading on a slightly rough circular cylinder: from subcritical up to high transcritical flow state. J Fluid Struct 2015;55:526–39.
[38] Schewe G. On the force fluctuations acting on a circular cylinder in crossflow from subcritical up to transcritical Reynolds numbers. J Fluid Mech 1983;133:265–85.
[39] Lefebvre S, Collu M. Preliminary design of a floating support structure for a 5MW offshore wind turbine. Ocean Eng 2012;40:15–26.
[40] Bagbanci H, Karmakar D, Soares CG. Comparison of spar-type and semi-submersible type floaters concepts of offshore wind turbines using long term analysis. In: Proc. Of the 32nd int. Conf. On ocean, offshore and arctic eng. Nantes, France; 2013.
[41] Robertson A, Jonkman J, Masciola M, Song H, Goupee A, C A, et al. Definition of the semisubmersible floating system for phase II of OC4. Tech. Rep. TP-5000-60601. NREL; 2014.
[42] Tran TT, Kim DH. Fully coupled aero-hydrodynamic analysis of a semi-submersible FOWT using a dynamic fluid body interaction approach. Renew Energy 2016;92:244–61.
[43] Liu YC, Xiao Q, Incecik A, Peyrard C, Wan DC. Establishing a fully coupled CFD analysis tool for floating offshore wind turbines. Renew Energy 2017;112:280–301.
[44] Musial W, Butterfield S, Ram B. Energy from offshore wind. In: Offshore technol. Conf. 2006 "new depths, new horizons". Houston, USA: Offshore Technology Conference; 2006. p. 1888–98.
[45] Sun X, Huang D, Wu G. The current state of offshore wind energy technology development. Energy 2012;41:298–312.
[46] Myhr A, Bjerkseter C, Ågotnes A, Nygaard T. Levelised cost of energy for offshore floating wind turbines in a life cycle perspective. Renew Energy 2014;66:714–28.
[47] van Hinsberg NP, Schewe G, Jacobs M. Experimental investigation on the combined effects of surface roughness and corner radius for square cylinders at high Reynolds numbers up to 10^7. J Wind Eng Ind Aerod 2018;173:14–27.
[48] Roshko A. Experiments on the flow past a circular cylinder at very high Reynolds number. J Fluid Mech 1961;10:345–56.
[49] Farell C. Flow around fixed circular cylinders: fluctuating loads. Journal of the Engineering Mechanics Division ASCE 1981;107:565–87.
[50] Desai A, Mittal S, Mittal S. Experimental investigation of vortex shedding past a circular cylinder in the high subcritical regime. Phys Fluids 2020;32:1–18. 014105.
[51] van Hinsberg NP, Schewe G, Jacobs M. Experiments on the aerodynamic behaviour of square cylinders with rounded corners at Reynolds numbers up to 12 million. J Fluid Struct 2017;74:214–33.
[52] Adams T, Grant C, Watson H. A simple algorithm to relate measured surface roughness to equivalent sand-grain roughness. Int J Mech Eng and Mechatron 2012;1:66–71.
[53] Theophanatos A. Marine growth and the hydrodynamic loading of offshore structures. Ph.D. thesis. Glasgow, United Kingdom: Strathclyde University; 1988.
[54] H. J. Allen, W. G. Vincenti, reportWall interference in a two-dimensional flow wind tunnel with consideration of the effect of compressibility, Tech. Rep. 782, Nat. Adv. Comm. Aero. Report (1944).
[55] Cao Y, Tamura T. Supercritical flows past a square cylinder with rounded corners. Phys Fluids 2017;29:1–17. 085110.
[56] Buresti G. The effect of surface roughness on the flow regime around circular cylinders. J Wind Eng Ind Aerod 1981;8:105–14.
[57] Lehmkuhl O, Rodríguez I, Borrell R, Chiva J, Oliva A. Unsteady forces on a circular cylinder at critical Reynolds numbers. Phys Fluids 2014;26(12):125110.
[58] Rodríguez I, Lehmkuhl O, Piomelli U, Chiva J, Borrell R, Oliva A. Numerical simulation of roughness effects on the flow past a circular cylinder. J Phys (Paris): Conf. Ser. 2016;745:1–8. 032043.
[59] Okajima A, Nakamura T. Flow around a circular cylinder with surface roughness in the high Reynolds number range. Tech. Rep. No. 40. Kyushuu Uinversity; 1973.
[60] Hu JC, Zhou Y, Dalton C. Effects of corner radius on the near wake of a square prism. Exp Fluid 2006;40:106–18.